

AN ABSTRACT OF THE THESIS OF

Matthew M. Tang for the degree of Master of Science in Radiation Health Physics presented on July 19, 2013.

Title: Progress in the Development of a Portable Phoswich-Style Skin Contamination Dosimeter.

Abstract approved:

David M. Hamby

The Code of Federal Regulations (10CFR20.1201) mandates occupational dose limits to the shallow, lens and deep tissue layers. The NRC-accepted procedure of estimating dose to these layers from contamination events is laborious. The current work aims to further the development of a portable phoswich-style skin dosimeter that will operate in real-time to determine dose to these tissue layers. A small dosimeter was designed, constructed, calibrated and tested. A hybrid pulse shape discrimination method and energy calibration technique for the three scintillation layers (BC-400, BC-444 and CaF₂) was developed. Measurements were compared against Monte Carlo (MCNP5) and deterministic (VARSKIN 5) simulations, and generally yielded results within 30% for the lens and deep layers. The current setup consists of a Field Programmable Gate Array (FPGA) based oscilloscope, with pulse shape discrimination and deposition measurements performed with the aid of a MATLAB algorithm. The system has a long system dead time which should be eliminated following application on an FPGA format.

©Copyright by Matthew M. Tang
July 19, 2013
All Rights Reserved

Progress in the Development of a Portable Phoswich-Style Skin Contamination
Dosimeter

by
Matthew M. Tang

A THESIS
submitted to
Oregon State University

in partial fulfillment of
the requirements for the
degree of

Master of Science

Presented July 19, 2013
Commencement June 2014

Master of Science thesis of Matthew M. Tang presented on
July 19, 2013

APPROVED:

Major Professor, representing Radiation Health Physics

Head of the Department of Nuclear Engineering and Radiation Health Physics

Dean of the Graduate School

I understand that my thesis will become part of the permanent collection of Oregon State University libraries. My signature below authorizes release of my thesis to any reader upon request.

Matthew M. Tang, Author

ACKNOWLEDGEMENTS

There are so many people to whom I am indebted that I don't know where to begin. First, I would like to thank my advisor Dr. David Hamby for his willingness to take me on as a graduate student. I also am grateful for his patience and guidance throughout the entire process. He has a great deal of wisdom and advice, but is always willing to listen before offering his opinions. I would like to express gratitude to Dr. Abi Farsoni for providing me with the equipment and resources necessary to perform the research. His opinions were greatly valued. I would also like to thank Dr. Oksana Ostroverkhova for giving us access to her laser lab. I would be remiss for failing to acknowledge Manfred Dittrich. He is a magician when it comes to building things. Most importantly, I would like to express love and gratitude to my wife, Alice, for supporting me and providing encouragement throughout the entire process.

TABLE OF CONTENTS

	<u>Page</u>
1. INTRODUCTION	1
2. LITERATURE REVIEW	3
2.1 Radiochromic Dye Films	3
2.2 Thermoluminescent Dosimeters (TLD)	4
2.3 Single Scintillator Systems.....	5
2.4 Phoswich Systems and Pulse Shape Discrimination.....	8
3. DOSIMETRY PHYSICS.....	13
3.1 Interactions with Matter	13
3.2 Photon Interactions.....	13
3.2.1 Photoelectric Effect	14
3.2.2 Compton Scattering	16
3.2.3 Pair Production	19
3.3 Beta Interactions.....	21
3.3.1 Direct Ionization and Delta Rays.....	21
3.3.2 Bremsstrahlung Radiation	22
3.4 Dosimetry System	23
3.4.1 Absorbed Dose	23
3.4.2 KERMA.....	24
3.4.3 Charged Particle Equilibrium	25
3.5 Dosimeter Components	26
3.5.1 Inorganic Scintillator	26
3.5.2 Organic Scintillator.....	27
3.5.3 Photomultiplier Tube (PMT)	29
4. DESIGN AND CONSTRUCTION	31
4.1 Scintillation and Absorber Design	31
4.2 Dosimeter Body Design and Photomultiplier Tube Selection	34

TABLE OF CONTENTS (Continued)

	<u>Page</u>
5. PULSE SHAPE DISCRIMINATION	42
5.1 Introduction	42
5.2 Fast-Slow Ratio Method.....	44
5.2.1 Methodology.....	44
5.2.2 Limitations.....	46
5.3 Pulse Fitting Method	47
5.3.1 Methodology.....	47
5.3.2 Limitations.....	53
5.4 Hybrid Fast-Slow Ratio Pulse-Fitting Method	56
5.4.1 Determining Threshold Values.....	58
5.4.2 Implementation.....	61
5.4.3 Limitations.....	63
6 DOSIMETER CALIBRATION	65
6.1 Introduction	65
6.2 CaF ₂ Layer Calibration.....	66
6.3 BC-444 Layer Calibration.....	68
6.4 BC-400 Layer Calibration.....	70
7 RESULTS AND DISCUSSION	73
7.1 Calibration Sources	73
7.2 Monte Carlo Dose Rate Calculation Method	73
7.3 Measurement of Dose Rate	74
7.4 Error Analysis	77
7.5 Dose Rate to Deep Tissue	78
7.6 Dose Rate to Lens of the Eye	81
7.7 Dose Rate to Shallow Tissue.....	81
8. CONCLUSION AND FUTURE WORK.....	83

TABLE OF CONTENTS (Continued)

	<u>Page</u>
BIBLIOGRAPHY.....	86
APPENDIX.....	90

LIST OF FIGURES

<u>Figure</u>	<u>Page</u>
Figure 1: The relative importance of the three major photon interactions (taken from Evans, 1955)	14
Figure 2: Dosimeter response to photoelectric absorption (taken from Knoll, 2010)	15
Figure 3: Compton scattering of unbound electron at rest (taken from Turner, 2007).....	16
Figure 4: Dosimeter response to Compton scattering (taken from Knoll, 2010).....	18
Figure 5: Pair production of a gamma-ray with $h\nu \geq 1.022$ MeV (taken from Cember, 2009)	19
Figure 6: Dosimeter response to pair production (taken from Knoll, 2010)	20
Figure 7: Torturous path of a beta particle and delta ray generation (taken from Martin, 2006)	22
Figure 8: Bremsstrahlung radiation production (taken from Martin, 2006)	22
Figure 9: Incremental volumes (squares) surrounding volume of interest (central). The lines represent secondary charged-particles from interaction with primary radiation (taken from Shultis & Faw, 2000)	25
Figure 10: Energy band structure of inorganic scintillator (taken from Knoll, 2010).....	27
Figure 11: Energy levels of an organic molecule with π -electron structure (taken from Knoll, 2010)	28
Figure 12: Photomultiplier tube (taken from Hamamatsu, 2006).....	30
Figure 13: 10 cm ² scintillation assembly. Same sequence as in Table 4, starting left to right	34
Figure 14: 1 cm ² scintillation assembly. Same sequence as in Table 4, starting left to right	34
Figure 15: Light transmission through an acrylic absorber	36

LIST OF FIGURES (Continued)

<u>Figure</u>	<u>Page</u>
Figure 16: Dosimeter design with scintillation assembly (yellow), light guide (blue), PMT (green), and socket assembly (red) displayed.....	37
Figure 17: Oscilloscope shots of 20 signal pulses	37
Figure 18: Light transmittance of a machined acrylic absorber	39
Figure 19: Light transmittance of a stack of acrylic sheets	39
Figure 20: Light transmittance of machined acrylic with optical grease.....	40
Figure 21: Coincident pulse with fast, medium and slow components	43
Figure 22: Integration time intervals, T1, T2, and T3 (taken from Farsoni, 2012)	44
Figure 23: Two-dimensional scatter plot of fast and slow ratios (taken from Farsoni, 2012)	46
Figure 24: CaF2 (slow) pulse. Integral, S , represented as orange region	48
Figure 25: Coincident pulse where the orange region represents the integral, S , which contains only slow contributions	50
Figure 26: Coincident pulse with a slow fit (blue line)	50
Figure 27: Coincident pulse where the orange region represents the integral, S , which contains only medium contributions	51
Figure 28: Coincident pulse with a medium fit (blue line).....	52
Figure 29: Fast component following subtraction of medium component	52
Figure 30: Slow fit applied to a BC-444 (medium) pulse.....	53
Figure 31: Histogram of legitimate slow (upper-left), illegitimate slow (upper-right), and combined legitimate and illegitimate slow (bottom) from a ^{137}Cs source	55
Figure 32: Histogram of legitimate and illegitimate medium pulses from a ^{137}Cs source (left) and ^{60}Co source (right).....	56

LIST OF FIGURES (Continued)

<u>Figure</u>	<u>Page</u>
Figure 33: Two-dimensional scatter plot of fast and slow ratios for ^{137}Cs pulses; boundaries are shown	58
Figure 34: Percent of legitimate slow lost (blue) and illegitimate slow passed (red) as a function of threshold value for ^{137}Cs (left) and ^{60}Co (right)	59
Figure 35: Remainder (right) following subtraction of slow fit from a slow pulse (left)	60
Figure 36: Percent of legitimate medium lost (blue) and illegitimate medium passed (red) as a function of threshold value for ^{137}Cs (left) and ^{60}Co (right)	61
Figure 37: Two-channel digital pulse processor, DPP2.0	62
Figure 38: Hybrid fast-slow ratio pulse fitting pulse shape discrimination process	62
Figure 39: CaF_2 layer spectra of ^{137}Cs (blue), ^{22}Na (red), and ^{133}Ba (black)	66
Figure 40: Calibration curve for the CaF_2 layer	67
Figure 41: BC-444 spectra of ^{60}Co (blue) and ^{133}Ba (red)	68
Figure 42: MCNP5 ^{60}Co energy spectrum for the BC-444 layer	69
Figure 43: Calibration curve for the BC-444 layer	70
Figure 44: BC-400 spectra of ^{137}Cs (blue) and ^{241}Am (red)	71
Figure 45: Possible calibration curves for the BC-400 layer	72
Figure 46: The pulse height distribution from the CaF_2 scintillation layer of a ^{137}Cs source	74
Figure 47: Multiplication of the pulse height distribution in Figure 46 by the energy	75
Figure 48: Ratios of the mass-energy absorption coefficient for tissue and calcium fluoride as a function of energy (taken from NIST, 1996)	80
Figure 49: Ratios of the mass stopping power for tissue and calcium fluoride as a function of energy (taken from NIST, 1998)	80

LIST OF TABLES

<u>Table</u>	<u>Page</u>
Table 1: Occupational effective dose equivalent limits mandated by the NRC (taken from NRC, 1991)	1
Table 2: Scintillation assembly design recommendations (taken from Cazalas, 2009) ...	31
Table 3: Composition and thicknesses of Mix A (taken from Cazalas, 2009)	32
Table 4: The material and thicknesses actually used	32
Table 5: The spectral range and peak wavelength of scintillators and PMT	35
Table 6: Spectral features used in the calibration of the CaF ₂ layer	67
Table 7: Spectral features used in the calibration of the BC-444 layer	70
Table 8: Possible spectral features used in the calibration of the BC-400 layer.....	72
Table 9: Approximate activities of the sources used for dose measurements	73
Table 10: Dead time measurement using the two-source method	76
Table 11: Dose rate comparisons for deep tissue.....	78
Table 12: Dose rate comparisons for eye-lens dose.....	81
Table 13: Dose rate measurements of shallow dose using calibration equations 1 through 3.....	82

PROGRESS IN THE DEVELOPMENT OF A PORTABLE PHOSWICH-STYLE SKIN CONTAMINATION DOSIMETER

1. INTRODUCTION

In modern society, the peaceful application of nuclear technology is ubiquitous. Uses range from energy generation to the health care industry. Despite being a boon to society, radionuclides and the products of nuclear fission are inherently harmful, capable of causing both deterministic and stochastic health effects (Hall, 2012). In an effort to reap the benefits of ionizing radiation, while preventing deterministic effects and mitigating the risk of stochastic effects, radiation dose limits have been extensively studied by the International Commission on Radiological Protection (ICRP) and the National Council on Radiation Protection (NCRP). In the United States both groups provide recommendations while the Nuclear Regulatory Commission (NRC) mandates. The occupational dose limits, established by the NRC, to the shallow, lens and deep tissue layers are tabulated in Table 1.

Table 1: Occupational effective dose equivalent limits mandated by the NRC (taken from NRC, 1991)

Layer	Density Thickness (mg cm⁻²)	Depth (cm)	Dose Limit (Sv)
Shallow	7	0.007	0.5
Eye Lens	300	0.300	0.15
Deep	1000	1	0.5

Determining dose to these tissue layers from radioactive contamination is a difficult task. If the contamination can be recovered, characterization is possible. The

laborious characterization process includes activity assay and physical sizing. These parameters can then be used to assess dose. (Soares, 1991)

The current work attempts to design, build, and calibrate a small phoswich-style prototypic dosimeter that is able to estimate the absorbed dose to the shallow, lens and deep tissue layers. The dosimeter contains three scintillators (BC-400, BC-444 and CaF₂) situated between tissue equivalent absorbers, allowing dose estimation for the shallow (7 mg cm⁻²), lens (300 mg cm⁻²), and deep (1000 mg cm⁻²) tissue layers, respectively. The scintillators are mated with a photomultiplier tube, with the anode output fed into a digital pulse processor. Pulses are processed by a MATLAB algorithm which performs the pulse shape discrimination and energy spectrum processes. This work developed a pulse shape discrimination process that allows energy to be attributed to the correct scintillator. Measured doses are compared with available software (e.g. VARSKIN 5 and MCNP5). The work presented here does not represent the endpoint. The final dosimeter is envisioned to be portable and fully integrated on a Field Programmable Gate Array (FPGA).

2. LITERATURE REVIEW

2.1 Radiochromic Dye Films

The use of radiochromic foils and extrapolation chambers (ECH) for hot particle dosimetry was investigated by Soares et al. (1991). Radiochromic foils, which underwent a color change upon irradiation, are read using a scanning laser microdensitometer at a wavelength of 633 nm. The foils were calibrated using $^{90}\text{Sr}/^{90}\text{Y}$ betas and ^{60}Co gamma rays. It was found that changes in absorbance at 633 nm were nearly linear between 0.5 to 1.2 kGy. Additional dose measurements were performed on an ECH based on a design by Loevinger and Trott (1966). The authors concluded that the use of ECH for the measurement of dose rates from small particle sources was problematic because the optimal particle position can be obtained only through trial and error. Comparisons between estimated dose rates showed a trend toward better agreement as the chamber's electrode size increased. This work differs from the current in that no attempts were made to measure dose to the tissue depths of interest.

The work by McWilliams et al. (1992) was an initial attempt to standardize hot particle dosimetry. Cobalt-60 spheres ranging from 50 to 300 μm in diameter were produced and dose rates for three hot particles were measured using radiochromic dye films (RDFs) and an extrapolation chamber (ECH). Additional methods included extended point kernels such as the NRC standard VARSKIN, ionization chamber and thin element dosimeters. This work differs from the current in that no attempts were made to measure dose to the tissue depths of interest.

Villarreal-Barajas et al. (2003) performed a comparative evaluation of depth-dose distributions from hot particles for ECHs, RDFs, and MCNP4B. Measurements were made using standardized ^{60}Co hot-particle sources. To achieve depth-dose distributions for the ECH, absorbing layers were placed between the source and the window. Depth-dose distributions for RDFs were performed by exposing a stack of RDFs to the hot particle source. The measured optical density was converted to dose rate, as a function of radial distance, using a calibration curve. The experimental setup for the ECH and RDF measurements were modeled as realistically as possible in MCNP4B simulations. ECH and RDF measurements agree well ($\pm 20\%$) at the surface, but deviations increase with depth, possibly from differing gamma radiation response. MCNP4B calculations and measurements agreed to within 25% for the averaging areas and depths considered, except for measurements made with the 3 mm collecting electrode. This work differs from the current in that the RDFs are a relative dosimeter; they require a dose response function.

2.2 Thermoluminescent Dosimeters (TLD)

The use of thermoluminescent dosimeters (TLD) for three-dimensional dose mapping of hot particles was compared to EGS4-Presta calculations evaluated by Setzkorn et al. (1997). Their hot particle source consisted of a 193 μm diameter sphere composed of a mixture of ^{60}Co and various metals. The TLD was a 50 μm thick layer of CaSO_4 deposited on a 50 μm Kapton plate. Measuring a lateral dose distribution requires only one TLD, while a depth-dose distribution requires a stack of TLDs. The TLD geometries used for both lateral and depth-dose distributions were simulated in EGS4.

Comparisons of depth dose at the center of the detector indicated that the EGS4 calculations were lower than the TLD measurements by a factor of 2.2. The authors attribute the difference to approximations made during the calculations. Taking this into account, the authors judged that a reasonable agreement was shown for the dose rate profile curves for both TLD measurements and EGS4 calculations. TLD foils were deemed an attractive method for dose-distribution measurements for hot particles. This work differs from the current in that the TLDs are a relative dosimeter; they require a dose response function.

Durham et al. (1991) evaluated the use of exoelectron dosimeters (EEDs) for measuring the shallow and deep dose. Exoelectron dosimeters are similar to TLDs. The addition of tissue-equivalent layers makes EEDs suitable for measuring the dose to the shallow, lens and deep layers. The authors found that EEDs have an energy independent response to gamma rays above 200 keV, yet they under-respond to gamma rays below 200 keV. The dose response was found to be linear within 2% in the range of 0.1 to 100 mGy, making the EED suitable for non-accident use. Further evaluations suggest that EEDs provide accurate measurements of the dose rate from hot particles. While this work measures dose to the tissue layers of interest, it does not operate in real-time, and it is a relative dosimeter.

2.3 Single Scintillator Systems

The use of a beta radiation survey meter to measure absorbed dose rate independently of beta energy was studied by Bingo et al. (1979). The survey meter

utilizes a plastic scintillator to measure the absorbed dose rate to the epidermal (7 mg cm^{-2}) layer and to the fingers (40 mg cm^{-2}). Discrimination thresholds were chosen to selectively measure the absorbed dose for the target tissue. The dosimeter response was constant to within 10% for beta particles above 0.4 MeV. In their study, absorbed dose rates for skin ranged from 5×10^{-2} to $1 \times 10^3 \text{ mrad h}^{-1}$, and absorbed dose rates for fingers ranged from 3×10^{-2} to $1 \times 10^3 \text{ mrad h}^{-1}$. The survey meter was said also to be useful for monitoring surface contamination. Their dosimeter differs from the current work in that they use one scintillation layer, and cannot measure the lens and deep dose.

Martz et al. (1986) developed a dosimeter using a portable beta spectrometer containing a tissue-equivalent plastic scintillator. The device contained two interchangeable windows, either a thin Mylar or a thick Lucite window. Use of the thick Lucite window was applied when a gamma spectrum was desired, shielding betas while minimally attenuating high-energy gamma radiation. Otherwise, a mixed spectrum was collected when using the thin Mylar window. The beta energy spectrum was obtained by stripping the gamma contribution from the mixed spectrum. The energy deposited in the deep layer of skin was estimated from a summation of the product of the number of counts in each channel of the gamma spectrum by its respective calibrated energy value. The energy deposition to the shallow layer of the skin was calculated from a summation of the product of counts in each channel of the beta spectrum with a beta function, representing the energy deposition per particle, for each energy interval. The beta energy deposition function in their study was determined by an iterative computer program using data collected using extrapolation chambers. Their dosimeter calculates beta and gamma

dose rates with an accuracy of 25%, when using a correction factor. This setup requires the use of an expensive extrapolation chamber, and does not provide real-time dose calculations, rendering it inadequate for field use. In addition, this method was unable to calculate dose rates to the lens. Their dosimeter differs from the current work because of the implementation of a single scintillation layer.

Vapirev et al. (1996) tested two different methods of beta radiation dosimetry using a scintillation probe. The probe was a 3 cm thick stilbene scintillator coupled to a PMT. The authors evaluated both 'differential' and 'dE/dx' methods to measure beta radiation dose. The sources included $^{90}\text{Sr}/^{90}\text{Y}$ and ^{137}Cs of approximately 1000 Bq each. The results were compared with Monte Carlo calculations from Cross et al. (1991 and 1992). The author's results deviated from the Monte Carlo calculations by 20% on average, with a maximum of 44%. Their dosimeter differs from the current work in that they use one scintillation layer.

Aydarous et al. (2004) introduced a system for the measurement of spatial dose distributions around hot particles. Their setup included a plastic scintillator, BC-430, coupled with an intensified charge-coupled device (ICCD). An advantage of using an ICCD was its ability to provide the correct spatial registration of the incident light. The placement of tissue-equivalent materials also allows the setup to measure tissue dose. Calibration of the system was carried out by comparing the area-averaged dose rates from RDFs with the area-averaged count rate with the scintillator-ICCD system. The use of BC-430 scintillators thinner than $\sim 100 \mu\text{m}$ was found to be inappropriate for low dose

rate measurements using the setup. Three hot particles from cooled nuclear fuel were utilized for skin dose evaluations with both RDFs and the scintillator-ICCD system. Exposure times for the scintillator-ICCD system were shorter by a factor of 100, excluding the lengthy processing of RDFs. Effective dose rates ranged from 6 to 2000 Gy h⁻¹ and current configurations prevented the measurement of shallow dose. The scintillator-ICCD system tended to underestimate the dose relative to RDFs when the dose was averaged over small areas; doses averaged over areas greater than 1 cm² were in good agreement with RDF measurements. Advantages include good linearity, reproducibility, relatively high spatial resolution and rapid evaluation speeds.

Kriss (2004) developed and tested a radiation detector capable of performing beta dosimetry and spectroscopy. The detector contained a plastic scintillator, and was mated to a large-area avalanche photodiode (LAAPD). Pulse processing electronics and various software programs were utilized to analyze signal pulses. Dose measurements were compared to Monte Carlo (MCNP) simulations. Depending on geometry and source type, measured doses were within 50% of Monte Carlo simulations. Spectroscopy results were also compared to Monte Carlo simulations. The detector proved capable of recording beta spectra with endpoint energies greater than about 250 keV.

2.4 Phoswich Systems and Pulse Shape Discrimination

Johnson et al. (1983) developed a portable beta-gamma dose rate meter that estimates absorbed dose to tissue in the layer between 5 and 10 mg cm⁻² depth. The system contains a 5 mg cm⁻² plastic scintillator covered by a 4 mg cm⁻² Mylar window,

and backed by a 1 cm thick Lucite light guide which simulates the backscattering of underlying tissue. The scintillator was mated to photomultiplier tube and the entire system was surrounded by a delrin casing. Pulse shape discrimination was implemented in the analog circuitry to eliminate signal pulses that originated from Cerenkov light. Cerenkov light pulses were produced when incident radiation interacted with the light guide and photomultiplier tube. A complete separation of scintillator events from non-scintillator events was impossible. Therefore some scintillator events were lost during the discrimination process. Measurements indicated an excellent beta response over a wide range of energies. In addition, good response and linearity was observed for ^{137}Cs gamma-rays. However, dosimeter response to low-energy photons was problematic due partially to mass absorption coefficient differences between the light guide and tissue. Measurements of mixed beta-gamma fields were compared to thermoluminescent dosimeter measurements. The measurements agreed within 5%.

Hajnal (1986) developed a portable phoswich-style dosimeter that is also capable of operating as a beta spectrometer. The dosimeter has two different radiation probes. The first probe is a front-end gated total beta energy absorption spectrometer that is also used to measure the total beta absorbed dose. The second probe is used to determine the non-penetrating surface dose and the penetration depth dose. Each probe contains fast and slow plastic scintillators. The same type of logic and circuitry was used for both probes. The work performed by Hajnal (1986) differs from the current work in that his design only contains two scintillation layers instead of three. In addition, he doesn't attempt to measure dose to the shallow, lens, and deep tissue layers.

Research was conducted by Vasilev and Volodin (1996) to develop a separately determined dose from gamma radiation and beta radiation from a mixed beta/gamma field. They utilized a spectrometric method based on a phoswich scintillation design. The first scintillation layer consisted of a thin europium-doped calcium chlorate film layered on 7 mg cm^{-2} thick polycarbonate. The second layer consisted of bulk scintillator made of stilbene. Scintillator selection ensured good light output and substantial differences in the luminescence times to allow discrimination. An algorithm was applied to determine dose. Measurements of beta emitting sources such as ^{90}Sr , ^{90}Y , ^{204}Tl , and ^{147}Pm showed dose rates in the range of 10^{-9} to $3 \times 10^{-7} \text{ Gy s}^{-1}$. Experimental errors were less than 15% for a 50 second measurement time and less than 5% for a 400 second measurement time. Measurements of a mixed beta-gamma radiation field with a gamma background showed that it was possible to separate the beta and gamma absorbed doses when their ratios were 2:1 or greater.

The doctoral work of Farsoni (2007) introduced a novel method and system for simultaneous gamma-ray and beta-particle energy spectroscopy. In his work he used a triple-layer phoswich style detector containing BC-400, CaF_2 and NaI scintillation layers. The scintillating layers had significantly difference decay times, namely 2.4 ns, 940 ns, and 250 ns, respectively. The pulse shape discrimination was performed by an algorithm which calculates a fast and slow ratio for each pulse. The parameters required to calculate the ratios included the baseline value, maximum value of the pulse sample, and two five-sample averages of the pulse. An analysis of the fast and slow ratios was used as a method to determine which scintillation layer(s) had emitted the light pulse, and by

extension, interacted with the radiation. Seven different interaction scenarios are possible. Depending on the interaction scenario, the incident radiation (gamma-ray or beta-particle) could be identified, its pulse integrated, and the energy pulse height distribution updated. Only pulses satisfying three of the seven interaction scenarios were counted, with those satisfying the other four discarded. Farsoni designed a digital pulse processor (DPP), utilizing a Field Programmable Gate Array (FPGA), to perform digital preprocessing steps. The DPP interfaced with the host PC through a MATLAB algorithm which performed the discrimination and other processes.

The work performed by Cazalas (2009) paved the way for this work. He designed a phoswich-style dosimeter out of commercially available materials. The design included three scintillation layers (BC-400, BC-444, and CaF_2), spaced by near-tissue-equivalent materials to achieve the correct density thicknesses for the shallow, lens, and deep layers. The design was determined by performing MCNP comparisons of the dosimeter design to tissue using a variety of sources. After building the dosimeter, he calibrated each layer of the dosimeter separately, since he did not perform pulse shape discrimination. While calibration for the third layer (CaF_2) was straightforward, spectra from the first (BC-400) and second (BC-444) layers generally lacked features usually used for calibration, namely photopeaks. He utilized a modified approach to calibrate the first and second layers. His approach will be discussed in section 6.3. This method proved useful for the second layer, but could not provide a good linear calibration equation for the first layer. The measured doses were compared to MCNP and VARSKIN. The doses measured by

the dosimeter correlated well, except for the first layer which differed significantly. The large discrepancy was probably due to the calibration issue.

Additional work was performed by Farsoni et al. (2012) to apply real-time pulse shape discrimination for radioxenon measurement. In this work, they calculated similar fast and slow ratios, but utilizing a different method. They integrated the pulses by convolving a pulse with three triangular filters, each with appropriate peaking times. The three pulse integrations were then used to calculate the fast and slow ratios. Since each pulse was expected to have a distinctively different shape governed by its light decay constant, there will be significant differences in the fast and slow ratios. Each pulse was then plotted on a two dimensional plot of the fast and slow ratios. Pulses from each scintillation layer will occupy specific regions on the plot. By establishing appropriate boundaries encompassing these regions, a confident determination can be made of energy deposition location. Pulses falling between two or more regions represent interactions with more than one scintillator (coincidence event). The convolution method described above was performed in an MATLAB algorithm (offline), but the pulse was integrated by summation on the actual VHDL code for the FPGA (real-time) due to the longer amount of time required for the IP Core convolution.

3. DOSIMETRY PHYSICS

3.1 Interactions with Matter

As stated in the introduction, the objective of the skin contamination dosimeter and the associated pulse processing is to estimate dose to the shallow, lens and deep tissue layers. It is designed for the estimation of absorbed dose, whether the radionuclides emit beta and/or gamma radiation. The reason alpha particles are omitted is the short range of heavy charged particles (HCP), and alpha particles emitted by radioactive decay do not have enough energy to penetrate the dead layer of the skin. Hence they pose no risk when the exposure is external.

Absorbed dose refers to the deposition of energy from incident radiation to the target medium. Likewise, scintillation detector and dosimeter responses involve the deposition of energy in the scintillators. Therefore, it is crucial to understand the radiation interactions occurring in the dosimeter. A treatment of radiation interactions significant to dosimetry and detector physics is given in this chapter.

3.2 Photon Interactions

There are two types of photons of interest in dosimetry, x-rays and gamma radiation. These two photons differ only in their origin, x-rays originating from the de-excitation of orbital electrons while gamma-rays are emitted when a nucleus de-excites. The primary photon interactions with matter include the photoelectric effect, Compton scattering, and pair production. The type of photon interaction which occurs depends on the energy of the incident photon, and the atomic number of the absorbing medium.

Figure 1 displays the dominating photon interaction for a given energy and atomic number. (Lilley, 2001)

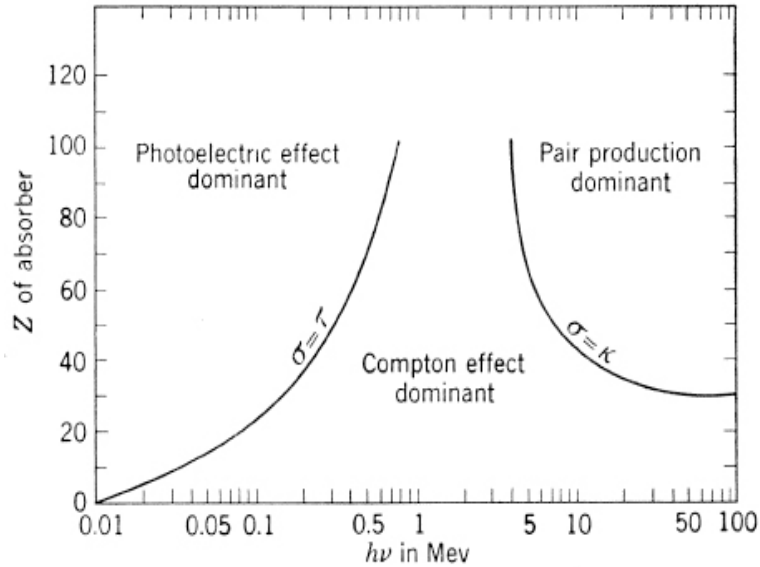


Figure 1: The relative importance of the three major photon interactions (taken from Evans, 1955)

3.2.1 Photoelectric Effect

The photoelectric effect occurs in the vicinity of an atom, where the energy of the photon, E_γ , is entirely converted to the liberation of a bound orbital electron, and its initial kinetic energy. The kinetic energy of the liberated electron, T , is given by,

$$T = E_\gamma - B_e \quad (1)$$

where B_e is the binding energy of the electron, commonly referred to as the work function. A portion of the photon's energy is required to overcome the binding energy, freeing the orbital electron. The remainder of the energy is converted to kinetic energy of the electron. The photoelectric effect can occur only with a strongly bound electron, as both energy and momentum cannot be conserved with a free electron. The probability of

photoelectric effect is dependent on the photon energy and atomic number of the target medium as given in the following equation. (Lilley, 2001)

$$\sigma_{pe} \propto \frac{Z^5}{E_\gamma^{3.5}} \quad (2)$$

Photoelectric absorption dominates for low-energy gamma radiation in high Z absorbers (Figure 1). The liberated electron can originate from multiple electron shells, but typically it originates from the K-shell. The resulting shell vacancy can be filled by a higher energy electron, emitting a characteristic x-ray. This process competes with the emission of an *Auger* electron. These characteristic x-rays can be absorbed through additional photoelectric interactions with less tightly bound electrons. If these x-rays do not escape the detector, the sum total of the kinetic energy of the photoelectrons created will equal the original energy of the incident photon. This is illustrated as a single full energy peak (Figure 2). Therefore, photoelectric is the preferred interaction when the intention



Figure 2: Dosimeter response to photoelectric absorption (taken from Knoll, 2010)

is the measurement of initial photon energy. The resultant full-energy peak is very important for calibration efforts, because it provides an easily recognizable feature in the energy spectrum which can be referenced to a specific photon energy. (Knoll, 2010)

3.2.2 Compton Scattering

According to the quantum model proposed by Compton, a photon of energy $h\nu$ with momentum $h\nu/c$ is incident on a stationary and unbound electron (Figure 3a). Following the collision, the photon scatters with an energy $h\nu'$, momentum $h\nu'/c$, and at angle θ relative to its original trajectory (Figure 3b).

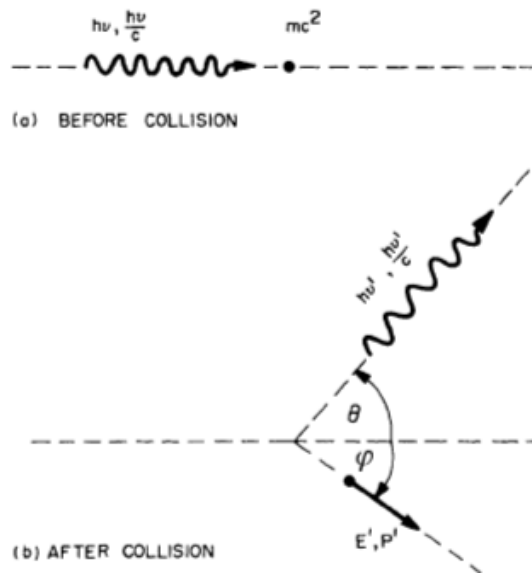


Figure 3: Compton scattering of unbound electron at rest (taken from Turner, 2007)

The electron recoils with angle ϕ , energy E' , and momentum P' . The shift in wavelength of the scattered photon (Compton shift) is given by the equation,

$$\Delta\lambda = \lambda' - \lambda = \frac{h}{mc}(1 - \cos\theta) \quad (3)$$

where h is Planck's constant, m is the electron mass, and c is the speed of light in a vacuum. The Compton shift is not dependent on the frequency ν of the incident photon. The energy of the scattered photon and recoiled electron can be found by considering that both energy and momentum are conserved. The energy of the scattered photon is dependent on the scattering angle and can be calculated with the following equation,

$$h\nu' = \frac{h\nu}{1 + (h\nu/m_0c^2)(1 - \cos\theta)} \quad (4)$$

where m_0c^2 is the rest energy of an electron (0.511 MeV). The kinetic energy of the recoiled electron, T , is the difference of the energies of the scattered and incident photons:

$$T = h\nu - h\nu' \quad (5)$$

Through substitution and algebraic manipulation the energy of the recoil electron is found with the following equation:

$$T = h\nu \frac{1 - \cos\theta}{m_0c^2/h\nu + 1 - \cos\theta} \quad (6)$$

The Compton electron reaches its maximum energy when a head-on collision occurs ($\theta=\pi$):

$$T_{max} = \frac{2h\nu}{2 + m_0c^2/h\nu} \quad (7)$$

In the other extreme, a grazing event occurs when $\theta \cong 0$, and $h\nu' \cong h\nu$. In this case, the recoil electron has energy $T \cong 0$, and $\varphi \cong \pi/2$. (Turner, 2007)

Compton scattering dominates in low Z absorbers and energies ranging from low to high energies (Figure 1). Since all scattering angles can occur in the active volume of the detector/dosimeter, a continuum of recoil electron energies can be produced. This continuum (*Compton continuum*) is shown in Figure 4. The value, E_C , is the energy gap

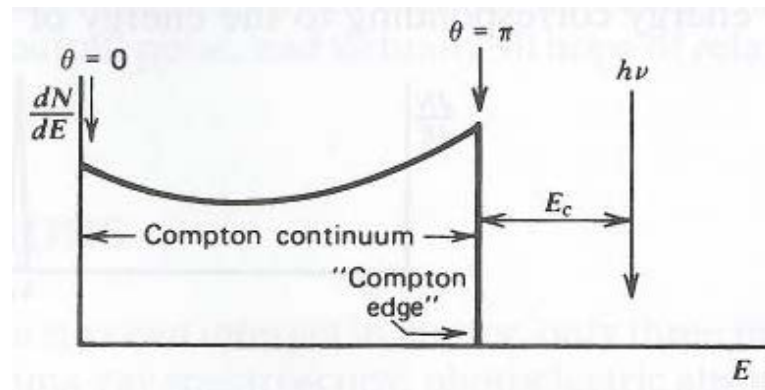


Figure 4: Dosimeter response to Compton scattering (taken from Knoll, 2010)

between the maximum Compton and the incident gamma and can be calculated using the following equation.

$$E_c = \frac{h\nu}{1 + 2h\nu/mc^2} \quad (8)$$

Because the orbital electrons are not exactly unbound or free, there will be measurable effects on the shape of the Compton continuum. These effects are a rounding-off of the rise in the continuum near its upper extreme, and a finite slope at the Compton edge instead of a sudden drop off. Although the Compton edge isn't as sharply defined as

idealized, it provides an important feature for the energy calibration. The Compton edge should be a distance of E_c from the energy of the incident gamma which is located by the full-energy peak. (Knoll, 2010)

3.2.3 Pair Production

A photon in the field of an atomic nucleus, with an energy of at least twice the electron rest energy $h\nu \geq 2mc^2 = 1.022 \text{ MeV}$ can be converted into an electron-positron pair (Figure 5). This same process can occur in the field of an electron, however the probability is significantly less, and the photon's energy must be at least four times the electron rest energy, $h\nu \geq 4mc^2$.

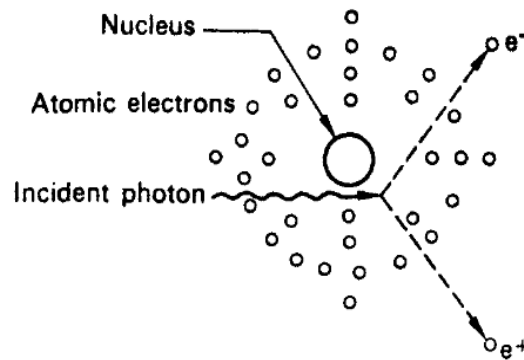


Figure 5: Pair production of a gamma-ray with $h\nu \geq 1.022 \text{ MeV}$ (taken from Cember, 2009)

Pair production that occurs in the field of an atomic nucleus will impart negligible energy to the massive nucleus. Thus, virtually all of the photon energy is converted to the electron-positron pair, and their initial kinetic energies.

$$h\nu = 2mc^2 + T_+ + T_- \quad (9)$$

The kinetic energy of the pair is not equally shared; the distribution of the excess energy between the electron and positron is continuous. The energy spectrum is identical for the two, and depends on the atomic number of the nucleus. The positron slows down, attracts an electron, and forms an electron-positron pair orbiting about their center of mass. This electron-positron pair is called positronium, and exists for approximately 10^{-10} seconds before the electron and positron annihilate. Upon annihilation, two 0.511 MeV photons are produced going in opposite directions to conserve momentum. Occasionally, the positron may decay in flight, with the energies of the photons totally 1.022 MeV in addition to the positron's kinetic energy. (Turner, 2007)

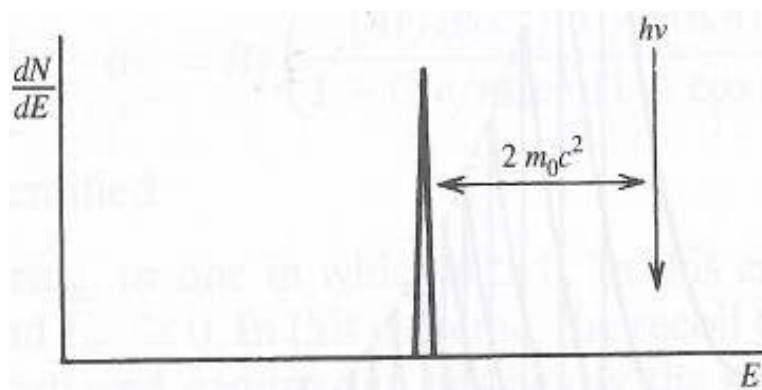


Figure 6: Dosimeter response to pair production (taken from Knoll, 2010)

Pair production dominates in high Z materials and high-energy photon radiation. A pulse height spectrum of the total kinetic energy imparted to the electron-positron pair by the incident gamma-ray is shown in Figure 6. The peaks represent a delta function at 1.022 MeV below the incident photon energy. Oftentimes, one or both annihilation photons escape resulting in single and double escape peaks located mc^2 or $2mc^2$ lower than the full-energy peak. (Knoll, 2010)

3.3 Beta Interactions

Beta particles are high-speed electrons emitted from nuclei during radioactive decay of neutron rich nuclides. Due to its minuscule mass, a beta with approximately 1 MeV has a velocity near the speed of light. Beta particles interact and deposit energy in a medium through direct ionization, delta rays, bremsstrahlung and Cerenkov radiation. The first three are discussed in this section. Cerenkov radiation is omitted because of its insignificance in dosimetry. (Martin, 2006)

3.3.1 Direct Ionization and Delta Rays

Because of its charge, a beta particle possesses a Coulomb electric field extending outwards radially. As a result, the beta will experience a Coulomb force with the electrons and nucleus of every atom it passes. This Coulombic force and its kinetic energy are such that an orbital electron can be liberated from the absorbing medium, creating an ion pair. This process is called ionization. Thus, beta particles lose energy as they ionize the atoms of the absorbing medium. Because of the high interaction probability, beta particles deposit their energy essentially at the interaction site. Beta particles have the same mass as the bound electrons with which they interact. As a result, they are deflected, forming a torturous path (Figure 7) instead of the linear paths seen with heavy charged particles. Along the beta particle's path, ionized orbital electrons may receive enough energy (on the order of 1 keV or more) that they may ionize additional atoms. These are called delta rays. They ionize other atoms of the medium along a route extending from the path of the beta particle as shown in Figure 7. (Martin, 2006)

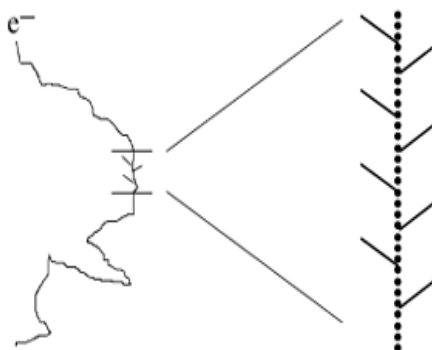


Figure 7: Torturous path of a beta particle and delta ray generation (taken from Martin, 2006)

3.3.2 Bremsstrahlung Radiation

In addition to collisional energy loss, electrons may lose energy via radiative means. As a beta particle passes near a nucleus, it experiences a Coulomb attractive force. This force causes the beta particle to accelerate, and the associated kinetic energy is lost as bremsstrahlung photons (Figure 8). Since beta particles from a source may approach a target atom's nucleus at many different angles, a spectrum of bremsstrahlung energies is produced. The yield of bremsstrahlung radiation

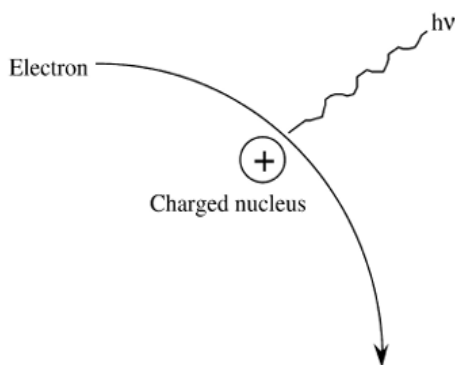


Figure 8: Bremsstrahlung radiation production (taken from Martin, 2006)

production is proportional to the kinetic energy of the electron and the atomic number Z of the absorbing medium. Tissue, which has a small effective atomic number, has less than a 1% probability of producing bremsstrahlung radiation when absorbing beta particles. Bremsstrahlung production is more significant in higher Z materials such as lead. (Martin, 2006)

3.4 Dosimetry System

An integral part of radiation protection is to establish a dosimetry system which includes well defined units for radiation dose. In the early days of radiation protection individuals relied on the so-called ‘paper-clip’ unit, when a shadow of an attached paper clip was detectable on a piece of dental film. For larger doses and radiotherapy, the “skin erythema” unit was applied. These units are not useful for radiation safety purposes because of their significant energy dependence, and other shortcomings. A different standard is necessary. (Cember, 2009)

3.4.1 Absorbed Dose

It has been determined that radiation damage to tissue is dependent on the absorption of energy from incident radiation, and is approximately proportional to the mean concentration of absorbed energy per unit mass in irradiated tissue. Absorbed dose is defined by the following equation.

$$\text{Absorbed Dose} = \frac{\Delta E}{\Delta m} \quad (10)$$

The concept of absorbed dose implies a uniform absorption of energy throughout the entire mass of tissue. Traditionally the unit for the absorbed dose was the *rad* which is defined as 100 ergs per gram. The rad has been replaced by the SI unit for absorbed dose called the *gray* (Gy). The gray is defined as one joule per kilogram (J kg^{-1}). One gray is equal to 100 rads. (Cember, 2009)

3.4.2 KERMA

KERMA is an acronym for *kinetic energy of radiation produced per unit mass in matter*. It is the quotient of the sum of the initial kinetic energies of the charged ionizing particles produced through interactions of indirectly ionizing radiation (e.g. x-rays and gamma radiation) and the mass of the target medium. This quantity is defined in equation (11),

$$K = \frac{d\bar{E}_{tr}}{dm} \quad (11)$$

and has the units of J kg^{-1} , not Gy. In principle KERMA differs from the absorbed dose in that it is the energy transferred, not absorbed, to the kinetic energy of all secondary charged particles. KERMA is oftentimes equal in magnitude to absorbed dose, and under the conditions of charged particle equilibrium they are equal. KERMA has no direct relation to biological effects of radiation, but it may be used with the hope of approximating the absorbed dose. It is a quantity that may be easily calculated using the following equation,

$$K = \phi E \left(\frac{\mu_{tr}}{\rho} \right) \quad (12)$$

where ϕ is the particle fluence, E is the energy of the indirectly ionizing radiation, and μ_{tr}/ρ is the mass energy transfer coefficient. (Shultis & Faw, 2000)

3.4.3 Charged Particle Equilibrium

As mentioned previously, charged particle equilibrium is a condition where the calculated KERMA may be used as an approximation for the absorbed dose. The condition of charged particle equilibrium is said to exist for incremental volumes wherein for every charged particle leaving the volume, another particle of the same type enters the volume with the same kinetic energy and direction. This is an idealization which, although is impossible to obtain exactly, may be approached under certain circumstances. This concept can be further understood by considering Figure 9. Charged particle equilibrium will not be established in the

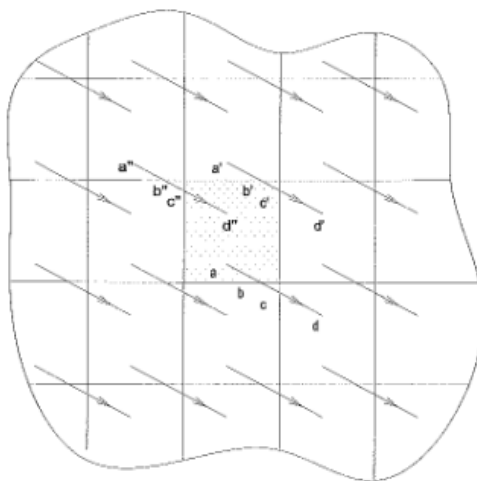


Figure 9: Incremental volumes (squares) surrounding volume of interest (central). The lines represent secondary charged-particles from interaction with primary radiation (taken from Shultis & Faw, 2000)

event that: (1) within the range of the more energetic particles, a boundary exists between the volume of interest and another medium of appreciably different properties. In this

case, the appropriate correspondence between similar tracks may not be established; and, (2) the primary radiation field varies appreciably within the volume surrounding the region of interest within the range of the most energetic secondary particles likely to be produced. In this case, a close correspondence between interactions and secondary particles in the volume of interest is unlikely. Even if both of these conditions do occur, the KERMA and absorbed dose may differ due to losses from bremsstrahlung, x-ray, and annihilation radiation. If the production of these tertiary indirectly ionizing radiations is negligible, KERMA can be utilized as a good approximation of the absorbed dose. Since the analytical determination of KERMA is much simpler than many means to estimate the absorbed dose, a strong incentive to utilize this approximation exists. (Shultis and Faw 2000)

3.5 Dosimeter Components

3.5.1 Inorganic Scintillator

The mechanism by which inorganic scintillators emit light depends on the energy states created by the crystalline lattice. In insulators or semiconductors, electrons reside only in discrete bands of energy (*valence* and *conduction*). The valence band represents those electrons which are bound at lattice sites. The conduction band represents those electrons which possess a sufficient amount of energy to migrate freely throughout the crystal. Electrons in a pure crystal cannot be found in the region between these two bands (*forbidden band*). These bands are represented in Figure 10. The addition of impurities called *activators*

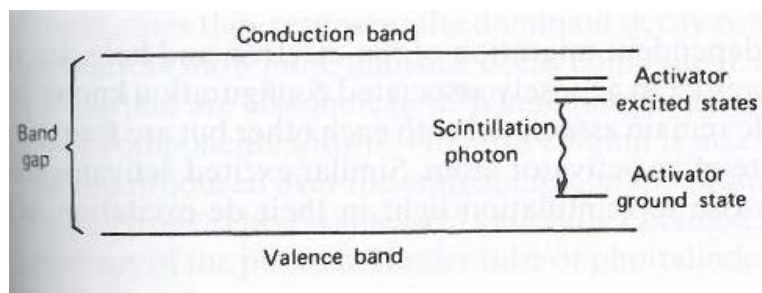


Figure 10: Energy band structure of inorganic scintillator (taken from Knoll, 2010)

form energy states within the forbidden band, from which electrons can de-excite and return to the valence band. The energy of the emitted photon is below the energy difference between the valence and conduction band. Thus, the scintillator is transparent to the emitted visible radiation. When ionizing radiation passes through the crystal, a large number of electrons-hole pairs will be formed. The positive holes quickly drift to an activator site, and ionize it because the activator ionization energy is lower. At the same time, the conduction band electron migrates throughout the crystal until it falls into the activator site, creating a neutral configuration with its own energy states. The relaxation of an electron from this activator energy state will emit visible radiation. (Knoll, 2010)

3.5.2 Organic Scintillator

Unlike inorganic scintillators which require a crystalline lattice as the basis for the scintillation process, the fluorescence process in organic scintillators arises from transitions in the energy level structure of a single molecule. The molecules of organic scintillators have an inherent symmetry property that gives rise to a π -electron structure. Consider Figure 11 which illustrates the π -electronic energy levels. Singlet states (spin

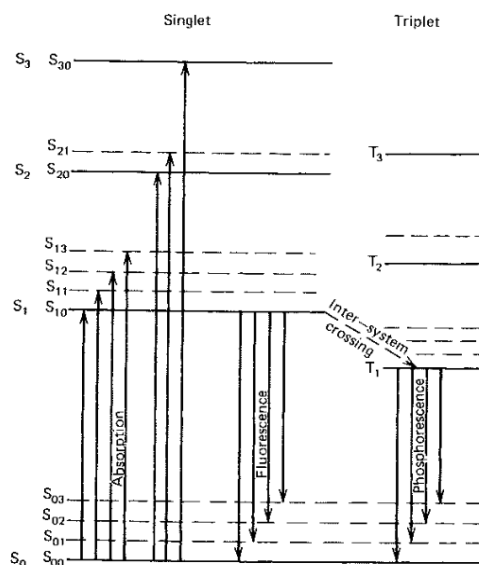


Figure 11: Energy levels of an organic molecule with π -electron structure (taken from Knoll, 2010)

0) are labeled as S_0, S_1, S_2 , and so on in the figure. The energy spacing between S_0 and S_1 states is about 3 to 4 eV, whereas the energy difference in higher energy states is less. Each configuration is subdivided into a series of finer spaced levels. These levels correspond to vibrational states, and a second subscript (e.g. S_{02}) is added to distinguish these vibrational states. When energy is absorbed, the electron configuration can be excited into any one of the excited states. Since average thermal energies are near 0.025 eV, nearly all molecules at room temperature are in the S_{00} state. The absorption of energy from interaction with radiation and the subsequent excitation is represented by the upward pointing arrows. Higher singlet electronic states quickly de-excite, through radiationless internal conversions, to the S_{10} state. In addition, states with excess vibrational energy (e.g. S_{02}) are not in thermal equilibrium with their neighboring molecules, and quickly lose their vibrational energy. The net effect of the excitation yields a population of excited molecules in the S_{10} state. When the molecule transitions

from the excited S_{10} state to any of the lower states, vibrational or S_{00} ground state, light is emitted. This process is known as prompt fluorescence. The transition is represented by a downward point arrow in the diagram. If the fluorescence decay time τ is known, the fluorescence intensity at time t can be calculated by the following expression. (Knoll, 2010)

$$I = I_0 e^{-t/\tau} \quad (13)$$

3.5.3 Photomultiplier Tube (PMT)

Photomultiplier tubes are used to convert the visible radiation emitted by the scintillators into an electrical signal. The photon passes through the glass and interacts with the photocathode. An electron is emitted via the photoelectric effect, and moves towards the dynodes. This liberated electron is accelerated and strikes the dynode, undergoing secondary electron emission. In secondary electron emission the energy deposited by the incident electron can result in the emission of more than one electron. Photomultiplier tubes have several dynodes which results in a cascade effect. The accumulated electrons (charge) are collected on the anode, resulting in an electrical signal. The anatomy of a basic PMT tube is shown in Figure 12.

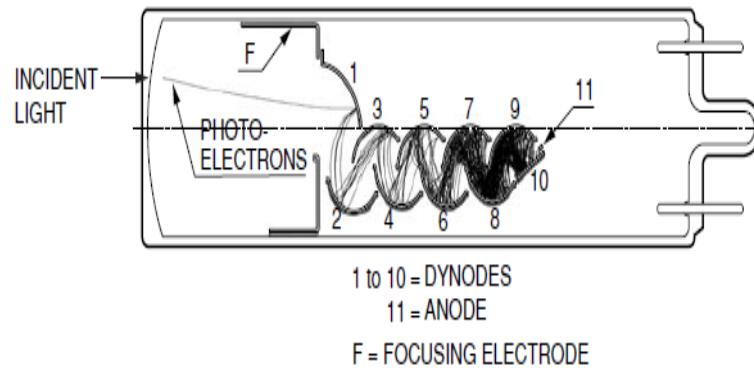


Figure 12: Photomultiplier tube (taken from Hamamatsu, 2006)

The overall gain, G , of a PMT tube is described by the following equation,

$$G = \alpha \delta^N \quad (14)$$

where α is the fraction of all photoelectrons collected by the multiplier structure, δ is the number of secondary electrons produced per incident photoelectron, and N is the number of dynodes. (Knoll, 2010)

4. DESIGN AND CONSTRUCTION

4.1 Scintillation and Absorber Design

The dosimeter design is partly based on the Master's thesis work of Edward Cazalas (Cazalas, 2009). The prototypic dosimeter that Cazalas built monitored only one depth (i.e. only one scintillation layer is present) at a time. At the time the ability to monitor multiple dose depth layers would require pulse shape discrimination which was beyond the scope of his research. Although that was the case, Cazalas provided recommendations for the design of a scintillation assembly (scintillators and tissue equivalent absorbers housed in an optically clear protective sheath). His design included three scintillation layers meant to provide an approximate absorbed dose to the shallow, lens and deep dose layers. His recommendations include the material and thicknesses as listed in Tables 2 and 3. These recommendations considered commercially available

Table 2: Scintillation assembly design recommendations (taken from Cazalas, 2009)

Layer	Material	Recommended Thickness		Running CL Total
		cm	mg cm ⁻²	mg cm ⁻²
Mylar	Mylar	0.00127	1.8	0.89
1 st Absorber	HDPE	0.0045	4.3	3.92
7 mg cm ⁻²	BC-400	0.002	2.1	7.09
2 nd Absorber	Mix A	0.218	262.1	139.2
300 mg cm ⁻²	BC-444	0.06	61.9	301.2
3 rd Absorber	Acrylic	0.508	602.0	633.2
1000 mg cm ⁻²	CaF ₂	0.06	190.8	1029.5
4 th Absorber	Acrylic	0.6	711.0	1480.4
	Total	1.44	1836	

Table 3: Composition and thicknesses of Mix A (taken from Cazalas, 2009)

Plastics	Mix A		
	PET	Acrylic	Total
Thickness (cm)	0.0152	0.2032	0.0152
Density Thickness (mg cm^{-2})	21.3	240.8	262.1

materials and standard thicknesses. More importantly, these recommendations were based on MCNP5 comparisons between the prototypic dosimeter and tissue. The simulated dose-region geometries were 10 μm thick tissue volume cylinders, large enough to ensure statistical soundness. (Sherbini, 2008)

In the current work, the above recommendations were followed as closely as possible. However, there is some variation due to the availability of the proposed materials and thicknesses (Table 4). The recommendation to use HDPE as the first

Table 4: The material and thicknesses actually used

Layer	Material	Thicknesses Used		Running CL Total
		cm	mg cm^{-2}	mg cm^{-2}
Mylar	Mylar	0.0004	0.552	0.276
1 st Absorber	FEP	0.00254	5.461	3.2825
7 mg cm^{-2}	BC-400	0.002	2.1	7.045
2 nd Absorber	Acrylic	0.2203	262.1	139.2
300 mg cm^{-2}	BC-444	0.06	61.9	301.2
3 rd Absorber	Acrylic	0.508	604.52	634.4
1000 mg cm^{-2}	CaF ₂	0.06	190.8	1032.1
4 th Absorber	Acrylic	0.6	714	1484.5
	Total	1.44	1836	

absorber material, for example, was not followed because of the unavailability of the film in the specified thickness. Instead the HDPE film was replaced with a fluorinated ethylene propylene (FEP) film, a transparent fluorocarbon similar to that of Teflon. FEP is a copolymer of tetrafluoroethylene (TFE) and hexafluoropropylene (HFP), with typical formulas containing 91.5 mol% and 8.5 mol% respectively. (Forsythe & Hill, 2000)

Ideally, dosimeters should be made of material that matches the medium of interest as closely as possible. If the materials are identical, then the dosimeter will be representative of the medium of interest in terms of interactions with radiation. (Attix, 1986) Therefore, it is essential that the effective atomic number is similar to that of tissue due. This is especially important in photon interactions because the mechanism of interaction (e.g. photoelectric, Compton scattering, and pair production) is strongly dependent on the atomic number of the absorber. An effective atomic number of 8.48 was calculated for FEP using the following equation,

$$Z_{eff} = (a_1 Z_1^\xi + a_2 Z_2^\xi + \dots)^{1/\xi} \quad (15)$$

where Z_i represents the atomic number of the i^{th} element of the material, and a_i its relative contribution to the electron density. (Wolbarst, 2005) The Mix A (Table 3) was replaced with an acrylic absorber because acrylic could be machined to the precise thickness needed. In addition, replacing the Mix A with a solid piece of acrylic would reduce the number of air gaps present, thereby increasing light collection.

Cazalas's design also included a protective sheath made of optically clear acrylic, with a thickness of 0.25 cm. The design adopted for this thesis combines the 4th absorber and the protective sheath into one single piece. This design allows all of the scintillators, and acrylic absorbers to be contained in a single structurally sound module, colored grey in the SolidWorks drawings of the 10 cm² and 1 cm² scintillation assemblies (Figures 13 and Figures 14).

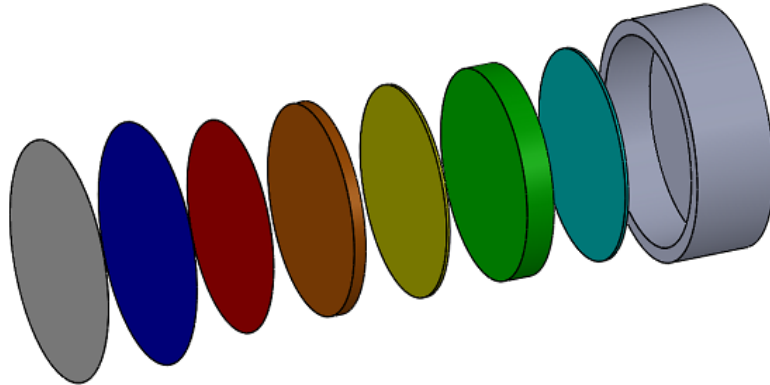


Figure 13: 10 cm² scintillation assembly. Same sequence as in Table 4, starting left to right

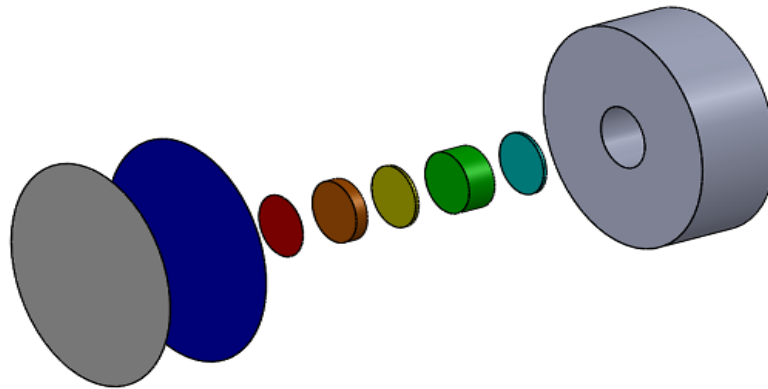


Figure 14: 1 cm² scintillation assembly. Same sequence as in Table 4, starting left to right

4.2 Dosimeter Body Design and Photomultiplier Tube Selection

The dosimeter is designed to be small and portable, thus a small photomultiplier tube (PMT) is desirable. Two of the most important factors to consider when mating a PMT to a scintillator are the spectral range and peak wavelength. The spectral range of the PMT should cover the spectral range of the scintillators, and its peak wavelength should be similar to that of the scintillators. The spectral range and peak wavelength for the three scintillator materials and PMT chosen are shown in Table 5.

Table 5: The spectral range and peak wavelength of scintillators and PMT

Component	Wavelength Spectral Range (nm)	Peak Wavelength (nm)	Decay time (ns)
BC-400	~350 to ~600	423	2.4
BC-444	~375 to ~530	428	285
CaF ₂	395 to ~525	435	940
R1924A	300 to 650	420	N/A

Because the PMT photocathode area is smaller than the face of the scintillation assembly, a light guide is required. A simple transparent conical frustum design has been chosen to function as a light guide. The light guide choice is important since absorption will reduce the overall light collection. Since the majority of the absorbers are made of acrylic, acrylic is the natural choice. Both scintillation assembly and light guide were wrapped in Teflon tape to increase light collection.

The fraction of light transmitted through the acrylic frustum $T(x)$ excluding losses due to reflection at the boundaries, can be calculated using Beer-Lambert's law,

$$T(x) = \frac{I(x)}{I_0} = e^{-\beta_a x} \quad (16)$$

where β_a is the optical absorption coefficient, x is the distance traversed, I_0 is the initial intensity and I is the intensity as a function of x . (Hecht, 1987) The absorption coefficient is dependent on the medium and is also a function of wavelength. The average peak emission wavelength for the 3 scintillation layers is approximately 429 nm. The optical absorption coefficient of light with a wavelength of 400 and 450 nm is 0.009 for acrylic. (Zwinkels, 1990) Assuming that the optical absorption coefficient is relatively constant between 400 and 450 nm, the transmittance can be calculated. The fraction of light transmitted is very high for thicknesses of a few centimeters (Figure 15). From these

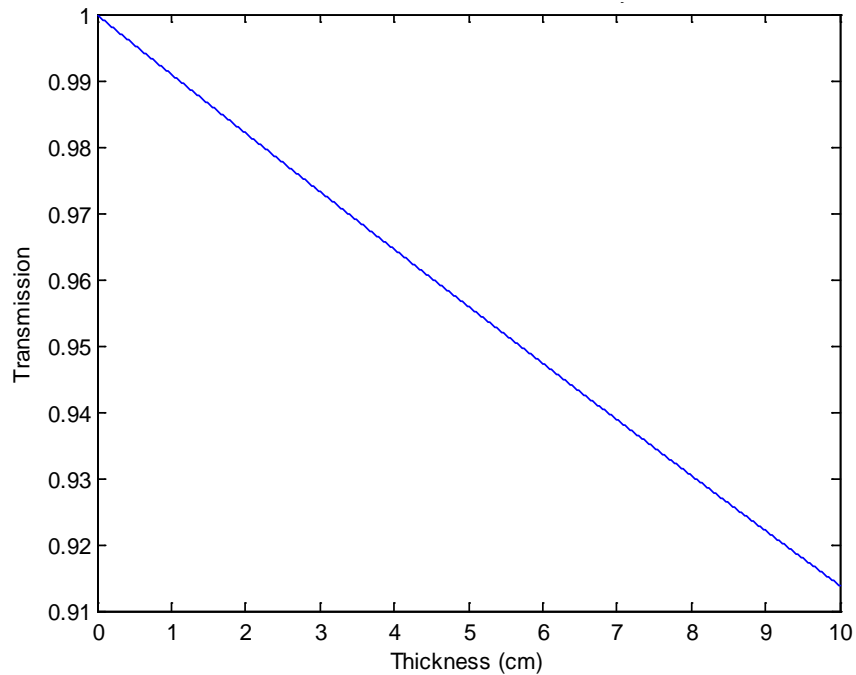


Figure 15: Light transmission through an acrylic absorber

calculations, it was determined that the conical frustum shaped light guide will result in a minimal reduction in light collection of approximately 3%.

A SolidWorks drawing of the dosimeter design is shown in Figure 16. The casing of the detector is designed using black acetal delrin. Delrin was chosen over a typical aluminum design for its lighter weight, and its ability to be machined easily. All of the components were built at the Oregon State University Engineering Service's machine shop.

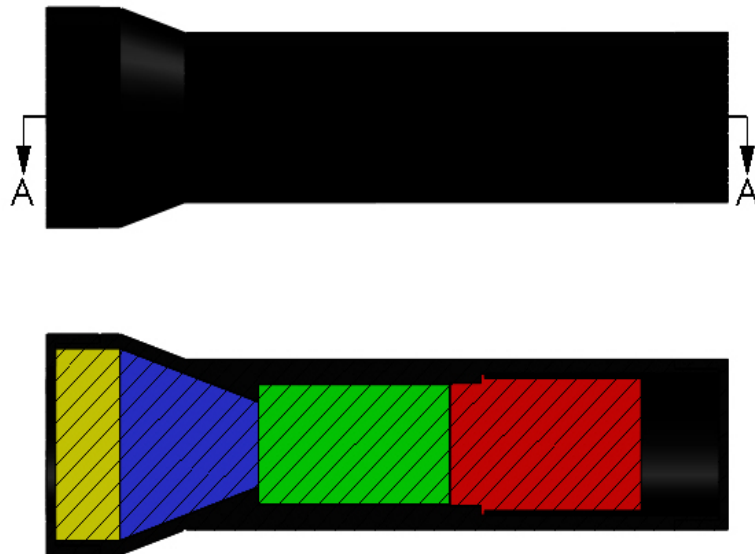


Figure 16: Dosimeter design with scintillation assembly (yellow), light guide (blue), PMT (green), and socket assembly (red) displayed

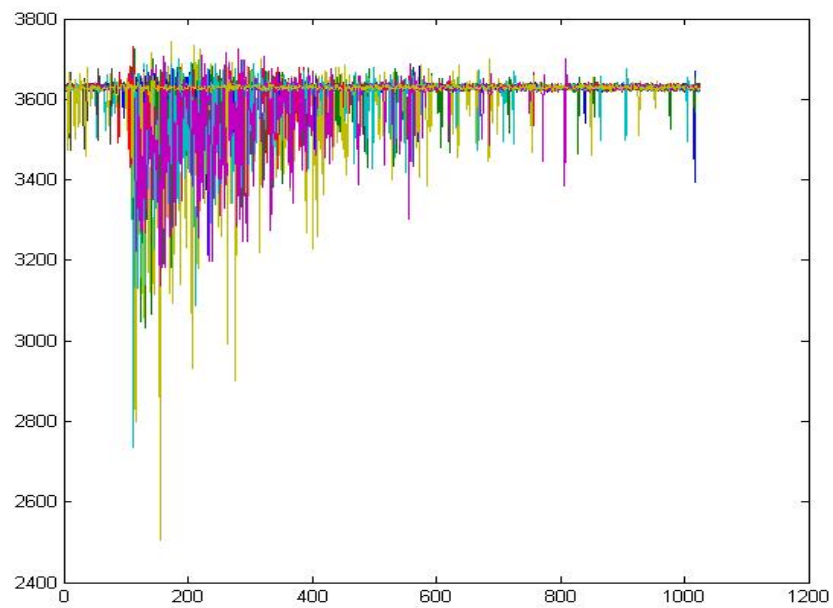


Figure 17: Oscilloscope shots of 20 signal pulses

After the device was assembled, initial tests were performed by viewing electrical signal pulses from the dosimeter through a digital oscilloscope (Figure 17). The pulses

were determined to be unsatisfactory. The pulses lacked proper waveforms, and there was a significant amount of overshoot. One possible cause of the malformations is thought to be poor light collection. One cause for the lack of light collection is the opacity of the absorbers. The acrylic absorbers had to be machined to the needed thicknesses using a lathe; clear acrylic sheets of the needed thickness are not commercially available. The machining process turns the formerly transparent acrylic translucent. The transmission of light through a machined acrylic absorber was measured at the Oregon State University Physics Department laser lab (Figure 18). The average light transmittance of the machined absorber was approximately 2%. The light transmission of a stack of two optically clear acrylic sheets was also measured (Figure 19). Although the transmission spectra are noisy up until approximately 500 nm, the average provides a good estimate of the light total transmission. The light transmission for the machined acrylic absorber is a factor of 40 lower than that of the stack acrylic sheets.

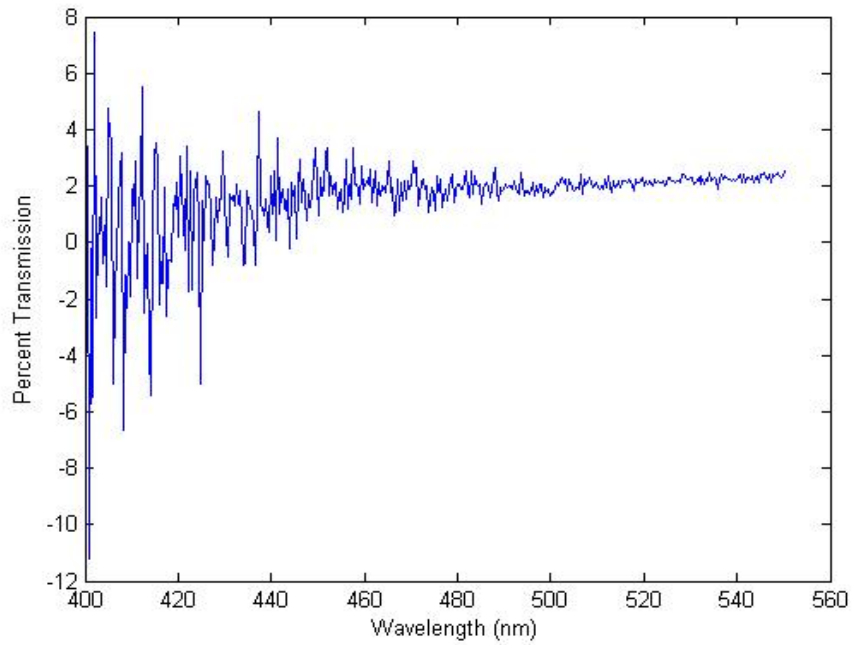


Figure 18: Light transmittance of a machined acrylic absorber

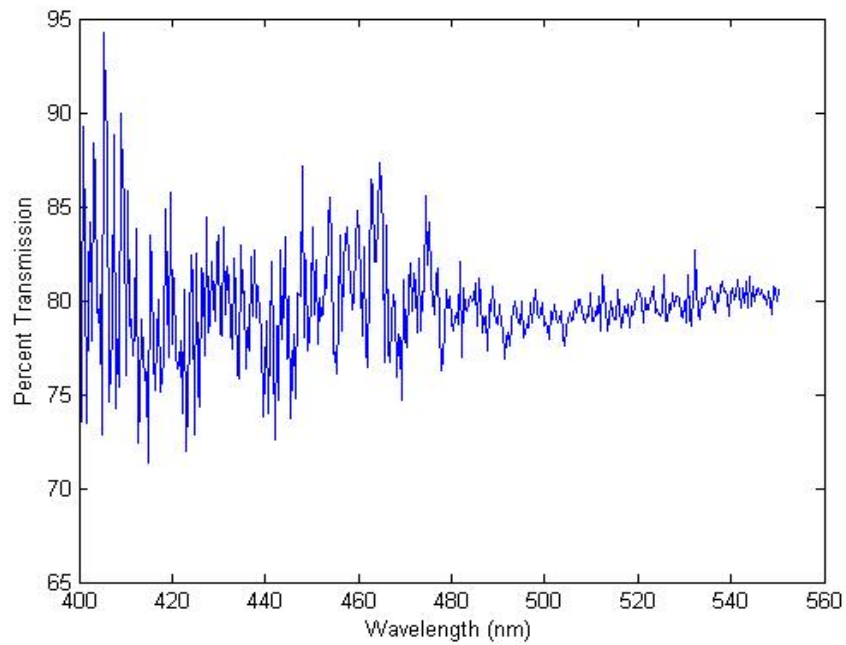


Figure 19: Light transmittance of a stack of acrylic sheets

There are several methods to recover the lost transparency. One option is to polish the surface until transparency is restored. This is a common industrial method. Cazalas utilized a different method to restore transparency. He used a heat gun to partially melt the surface of the machined acrylic. Upon recrystallization, clarity was restored. However, this approach is somewhat problematic. The corners and edges of the acrylic parts receiving the treatment tend to receive a larger amount of heat than the rest, and as a result become rounded. This is an undesirable outcome because some of the absorbers don't fit properly and gaps in the corners arise. A different solution to the problem involves adding a negligibly thin layer of optical grease. Although images seen through the treated acrylic were slightly distorted, the light transparency was restored as shown in Figure 20. It is noted that the average light transmission is higher than that of the stacked

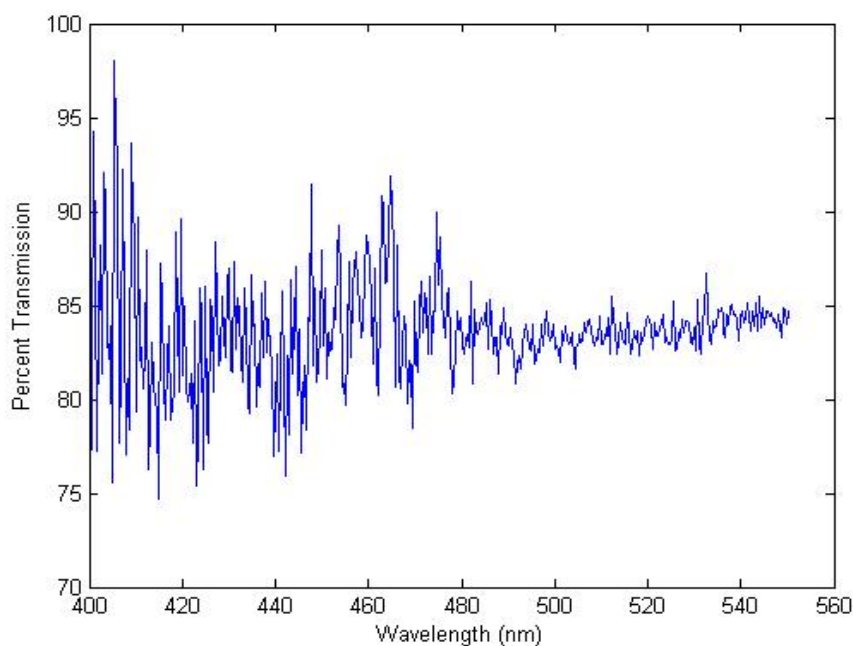


Figure 20: Light transmittance of machined acrylic with optical grease

acrylic sheets. The light transmission for the stacked acrylic sheets is lower because there are more boundaries that the light must traverse. With each boundary, a percentage of the light is reflected instead of being transmitted. The latter treatment method was selected because the grease is easy to apply, and because of the lack of physical changes to the machined absorbers.

After the treatment to restore transparency, there was a noticeable difference in visual clarity. However, the pulse waveforms were only slightly better. It was determined that the remaining issue could be either poor light collection from the light guide design or a malfunctioning PMT. The PMT is currently under inspection by the manufacturer. This obstacle was overcome by placing the scintillation assembly in Cazalas's casing. Using that case, there is no light guide and light collection is much more efficient. His design incorporates a larger PMT with a photocathode area that envelopes the entire assembly. Although his design is simpler, it is also bulkier. Work continues to investigate the operational characteristics of the smaller PMT, and light transmission characteristics of our frustum light guide design.

5. PULSE SHAPE DISCRIMINATION

5.1 Introduction

As stated earlier, the triple-layer phoswich dosimeter design has three scintillation layers, each with a unique light-decay characteristic. These three layers are meant to estimate the dose to the shallow, lens and deep layers of tissue. Scintillator selection was optimized with one of the requirements being obtaining the largest differences in decay time, resulting in distinctly different light-pulse shapes. Radiation incident on the dosimeter can interact with a single scintillation layer or multiple layers. The latter scenario is referred to herein as a coincident event. Typically, radiation interacts with only one scintillation layer, with interactions involving two layers occurring occasionally; interactions with all three scintillation layers are extremely rare. Coincident events involving two or three layers occur with these frequencies because of the low probability of interaction per scintillation layer, and because coincident events follow the multiplication rule of statistics. Furthermore, photons that interact in shallower scintillation layers may be scattered out of the path of deeper layers. Figure 21 illustrates a coincident pulse from simultaneous interactions with the fast, medium and slow scintillation layers.

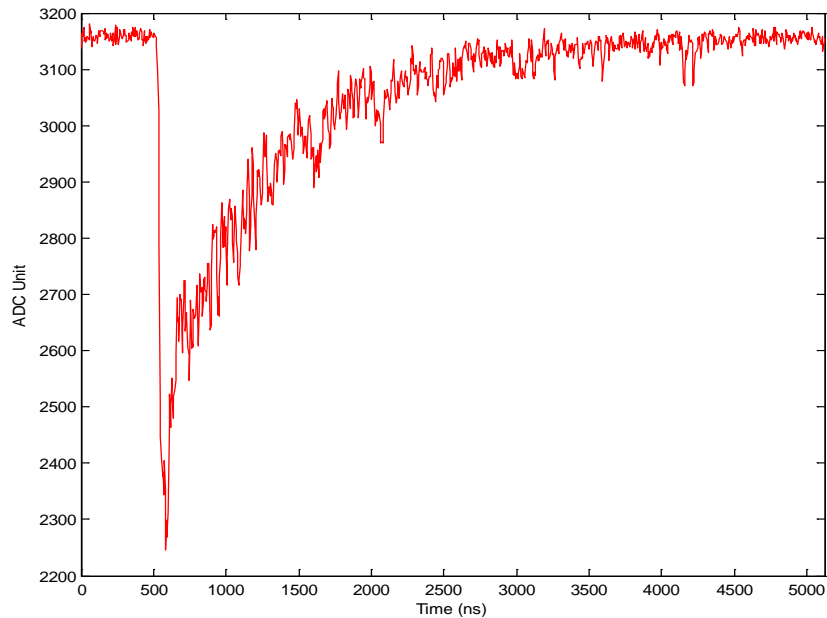


Figure 21: Coincident pulse with fast, medium and slow components

These differences in light-pulse shapes make it possible to determine which scintillator(s) were impacted by the radiation using techniques called pulse shape discrimination (PSD). When the scintillation layer(s) receiving energy deposition are identified, the deposited energy can be added to the energy spectra and the absorbed dose determination for the specific layer(s). If the dosimeter is truly representative of the target medium, then the absorbed dose to a given scintillation layer is a reliable estimation of the actual dose to the shallow, lens or deep tissue layers. Two pulse-shape discrimination methods are described, followed by the hybrid approach used in this work.

5.2 Fast-Slow Ratio Method

5.2.1 Methodology

To discriminate between the different pulse shapes, each pulse is integrated over three time intervals by convolution with three digital triangular filters, each tuned with appropriate peaking times. The triangular filter peaking times were chosen by considering the time required to integrate each pulse (approximately 4 to 5 times the light decay time), and the quality of the discrimination (i.e. good spatial separation). The time intervals, T_1 , T_2 and T_3 , over which pulses are integrated, are shown in Figure 22. The

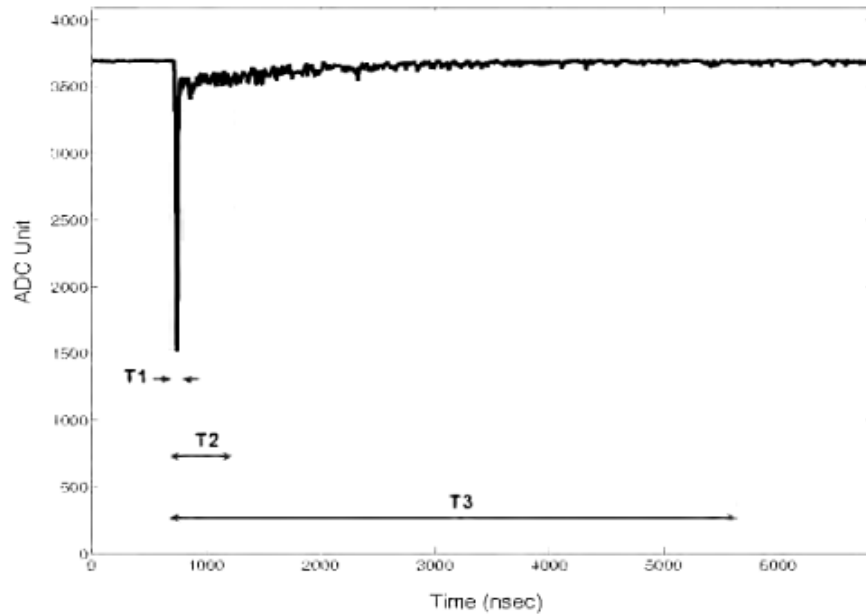


Figure 22: Integration time intervals, T_1 , T_2 , and T_3 (taken from Farsoni, 2012)

output amplitudes of the convolution process, S_1 , S_2 and S_3 , represent the integral of the signal pulse for time intervals, T_1 , T_2 and T_3 , respectively. These sums are used to calculate the fast and slow ratios using the following equations.

$$FCR = \frac{S_1}{S_2} \quad (17)$$

$$SCR = \frac{S_2 - S_1}{S_3 - S_1} \quad (18)$$

Ideally, the values of the fast and slow ratios should range from zero to unity. Integration, via the convolution process, may be replaced with a summation. This substitution is preferable when the discrimination process is performed real-time on a Field Programmable Gate Array (FPGA); the IP core convolution component requires more time, however, resulting in longer dead times. There are seven possible interaction scenarios with a triple-layer phoswich system. These scenarios are represented as seven regions on a two-dimensional scatter plot of fast and slow ratio (Figure 23). Boundaries can be set around the region for a particular interaction scenario. Pulses falling within the boundaries are identified as having originated from that specific layer, and the energy spectrum for that layer is updated. Coincident pulses will result in ratios that lie between these regions. This method is a simple yet powerful method to determine how incident radiation is deposited in the detector. (Farsoni, 2012)

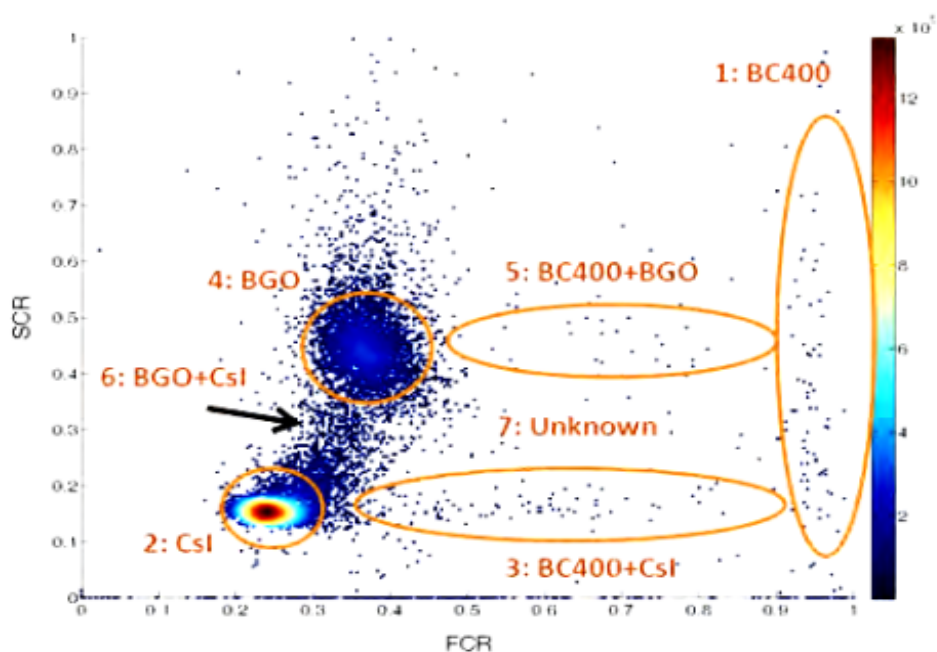


Figure 23: Two-dimensional scatter plot of fast and slow ratios (taken from Farsoni, 2012)

5.2.2 Limitations

The fast-slow ratio method is not perfect. The boundaries are somewhat arbitrary, and the region centroids are not fixed. The centroid position differs between radionuclides, making the use of fixed boundaries difficult. The fast-slow ratio method omits pulses that fall outside the boundaries and it does not offer the ability to measure coincident pulses since they also lie outside the boundaries. These exclusions make dosimetry measurements inaccurate since all energy deposition events are not included in the final dose estimate. Since this method cannot evaluate these pulses, a different method was considered.

5.3 Pulse Fitting Method

5.3.1 Methodology

The pulse fitting method essentially fits an exponential function to the signal pulse and determines its integral. This method requires that the pulse integral is known within a defined limit. Light emission from scintillation events is well understood, thus, fluorescence intensity can be modeled as an exponential decay function,

$$I(t) = I_0 e^{-t/\tau} \quad (19)$$

where t is the time following excitation, and τ is the fluorescence decay time. (Knoll, 2010) The area under the intensity curve is proportional to the energy absorbed in the scintillator and can be found by integrating equation (19) over the entire pulse,

$$\tilde{I} = I_0 \int_0^{t_2} e^{-t/\tau} dt \quad (20)$$

where t_2 is the integration time for the entire pulse, approximately 4 to 5 times the light-decay time. The only unknown variable is the initial intensity. The initial intensity can be calculated, however, if the integral, S , of the pulse within a defined limit is known (Figure 24).

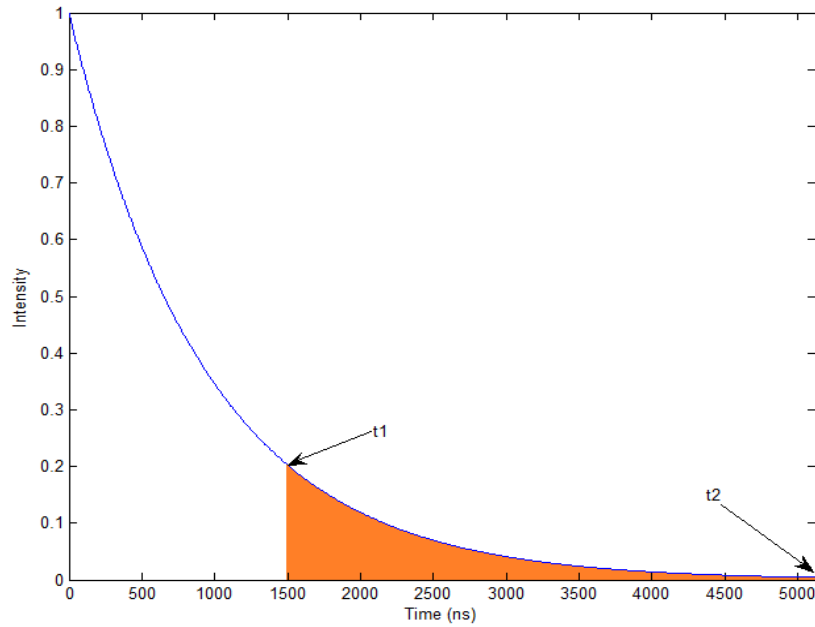


Figure 24: CaF2 (slow) pulse. Integral, S , represented as orange region

This can be calculated by integrating equation (19) over the defined limits:

$$S = \int_{t_1}^{t_2} I_0 e^{-t/\tau} dt = I_0 \int_{t_1}^{t_2} e^{-t/\tau} dt. \quad (21)$$

Then, the initial intensity can be found by algebraic manipulation of equation (21):

$$I_0 = \frac{S}{\int_{t_1}^{t_2} e^{-t/\tau} dt}. \quad (22)$$

In reality, S is unknown and the pulse is a discrete signal, sampled every 5 ns with a 200 MHz system. However, it may be approximated by performing a Riemann sum of the discrete pulse,

$$S \approx \sum_{i=n_1}^{n_2} f(i)\Delta t = \Delta t \sum_{i=n_1}^{n_2} f(i), \quad (23)$$

where $f(i)$ is the amplitude of the pulse at a particular sample n and Δt is the time between samples. The pulse fit and its integral can then be calculated with the following equations:

$$I(t) = I_0 e^{-t/\tau} = S \frac{e^{-t/\tau}}{\int_{t_1}^{t_2} e^{-t/\tau} dt} \approx \Delta t \sum_{i=n_1}^{n_2} f(i) \frac{e^{-t/\tau}}{\int_{t_1}^{t_2} e^{-t/\tau} dt} \quad (24)$$

$$\tilde{I} = I_0 \int_0^{t_2} e^{-t/\tau} dt = S \frac{\int_0^{t_2} e^{-t/\tau} dt}{\int_{t_1}^{t_2} e^{-t/\tau} dt} \approx \Delta t \sum_{i=n_1}^{n_2} f(i) \frac{\int_0^{t_2} e^{-t/\tau} dt}{\int_{t_1}^{t_2} e^{-t/\tau} dt}. \quad (25)$$

The pulse fitting method described above can also be used to analyze coincident pulses. Consider the coincident pulse shown in Figure 21. To estimate the slow component, the pulse region which excludes major contribution from the fast and medium layer is integrated first (Figure 25). An estimation of the entire slow component (slow fit) is then made using equation (24) (Figure 26). The integral of the slow fit is calculated using equation (25), and the slow component (Figure 26) is subtracted from the coincident pulse (Figure 25) leaving only the fast and medium components (Figure 27).

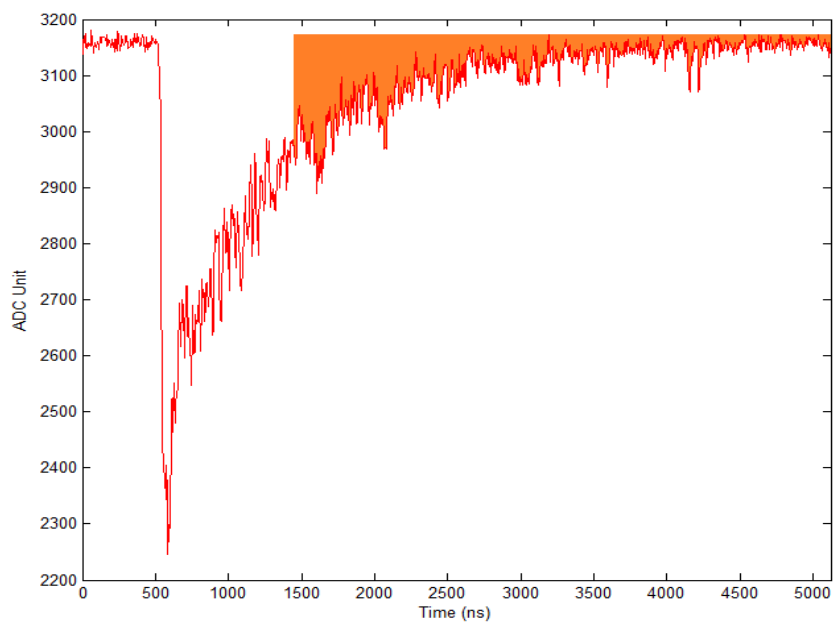


Figure 25: Coincident pulse where the orange region represents the integral, S , which contains only slow contributions

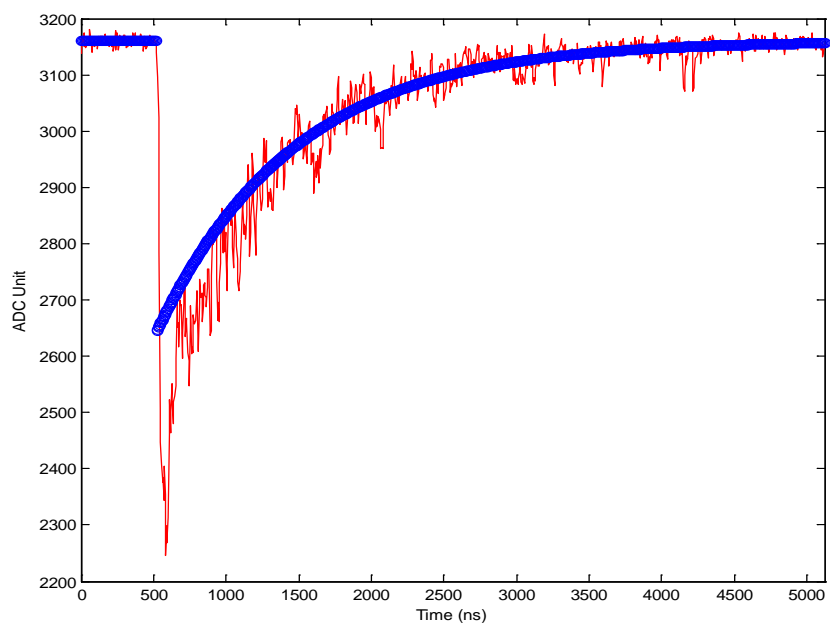


Figure 26: Coincident pulse with a slow fit (blue line)

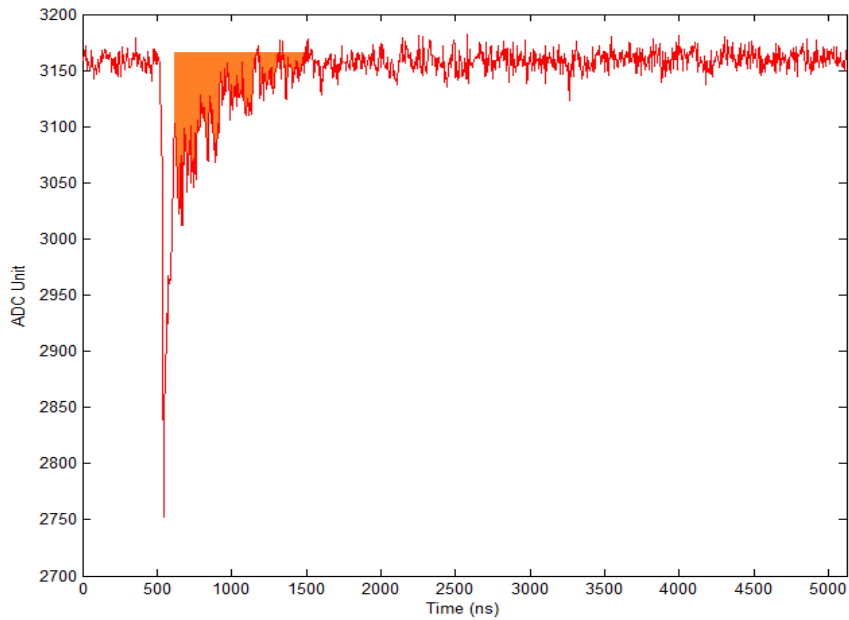


Figure 27: Coincident pulse where the orange region represents the integral, S , which contains only medium contributions

Once the slow component has been removed from the coincident pulse, the process will be repeated once again. An integration of the pulse excluding the fast component is carried out (Figure 27), a medium fit is applied (Figure 28) and the integral of the medium component is estimated. Ideally, after both slow and medium components have been removed, only the fast component remains (Figure 29). The integral of the fast component is then determined by performing a Riemann sum.

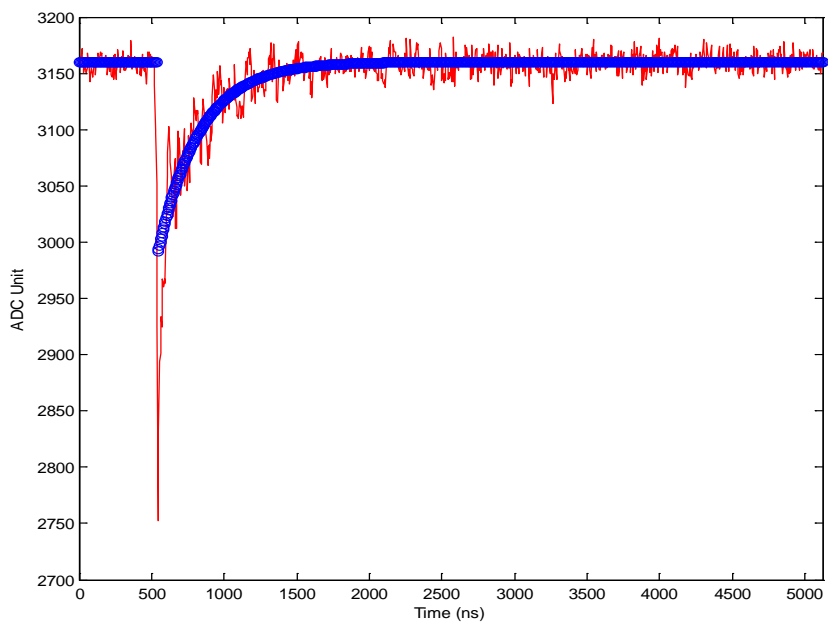


Figure 28: Coincident pulse with a medium fit (blue line)

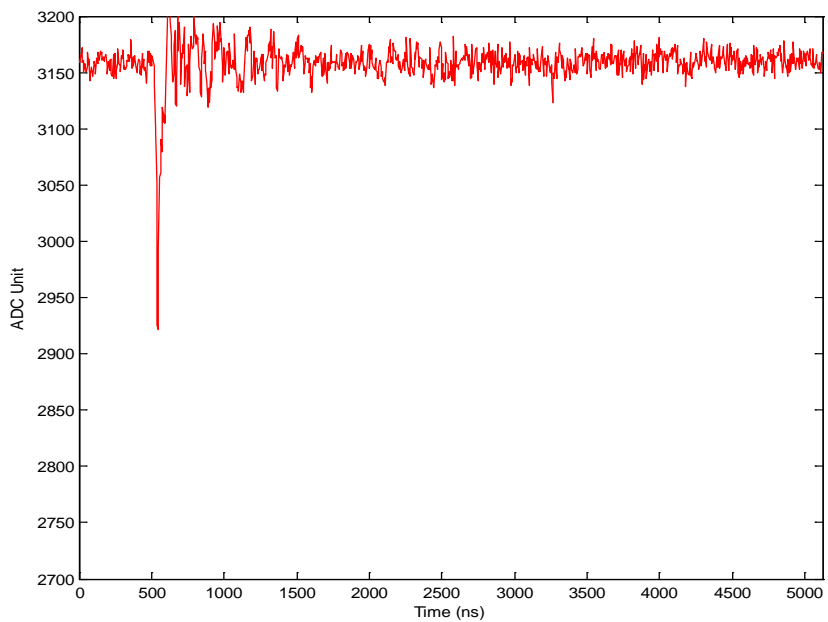


Figure 29: Fast component following subtraction of medium component

5.3.2 Limitations

The treatment provided above considers those extremely rare cases where radiation has interacted with all three scintillation layers of the dosimeter. A method, however, is required to determine if slow, medium and/or fast components are present. Consider the process of estimating the slow component. The pulse-fitting method works by integrating the region where only a slow component should exist. Suppose, however, the incident radiation interacts with the medium layer causing it to scintillate. If the summation region is noisy or has not returned to the baseline value following the medium pulse, the value of the summation may be larger than zero. When this is plugged into equations (24) and (25), a fit will be created and a positive area will be calculated (Figure 30). The pulse-fitting method will estimate a slow component although none is present.

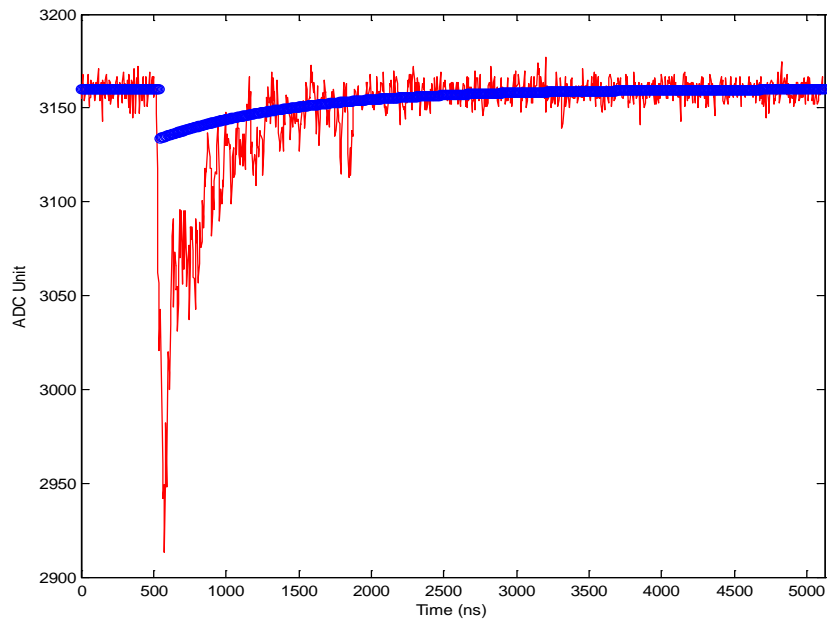


Figure 30: Slow fit applied to a BC-444 (medium) pulse

This can be problematic since not every pulse will be a slow pulse or contain a slow component. A method is required to distinguish legitimate slow pulses, or components thereof, from the illegitimate.

One method is to set a threshold value for the integral of the slow fit. If a slow component or pulse is absent, the integral of the fit would ideally be smaller than if a slow component or pulse was present. If the integral exceeds the threshold value then a slow component or pulse is present. Otherwise, the system proceeds to determine if a medium component or pulse is present.

The determination of the threshold value was attempted by first applying the pulse fitting method to exclusively calcium fluoride (slow) pulses. The tails were summed, a fit was made, and the areas were calculated using equation (25). These are considered the legitimate slow pulses. The same process was applied to strictly BC-444 (medium) pulses. These are the illegitimate slow pulses. The legitimate and illegitimate slow areas were plotted in a histogram of equation (25) (Figure 31). The two histograms were combined to determine if there is a good enough separation to apply a single threshold value for the integrals calculated using the pulse-fitting method (Figure 31). There is a considerable amount of overlap. A threshold that prevents the passing of illegitimate slow pulses, yet keeps legitimate slow pulses, is impossible. Additionally, the passing of illegitimate slow pulses will distort medium pulses.

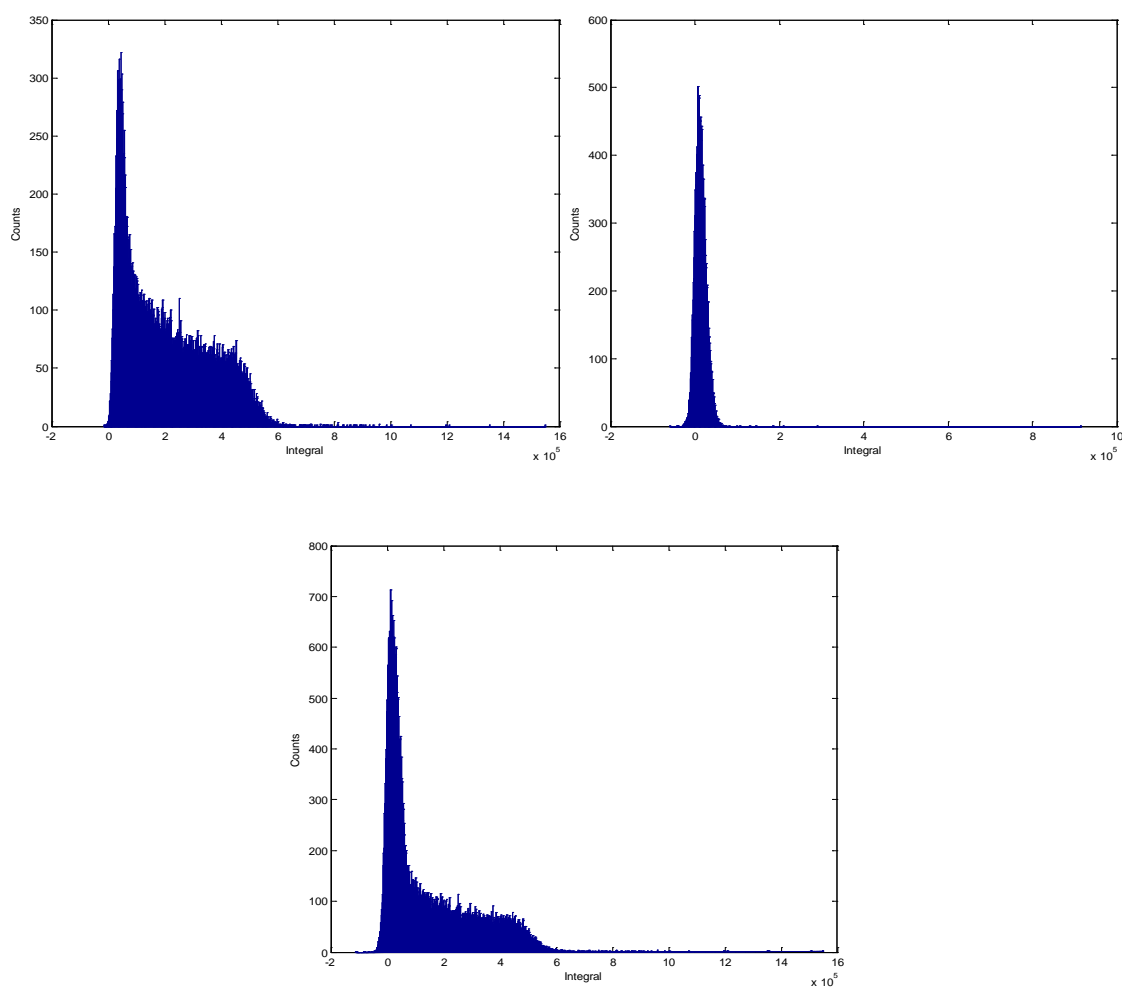


Figure 31: Histogram of legitimate slow (upper-left), illegitimate slow (upper-right), and combined legitimate and illegitimate slow (bottom) from a ^{137}Cs source

Consider the presence of only a medium pulse. If the baseline fails to return to the pre-trigger value, the integral of the slow fit may yield a positive value that exceeds the threshold. The slow component fit will be subtracted from the pulse, decreasing the amplitude of the medium pulse. Legitimate slow pulses that are lost will be counted as a medium pulse, further skewing the spectrum.

A threshold value for medium pulses is also required. The medium fit was performed for exclusively medium (legitimate) and fast (illegitimate) pulses. The areas of the legitimate and illegitimate medium pulses were calculated using equation (25) and plotted in a histogram (Figure 32). A good separation exists. The presence of a medium

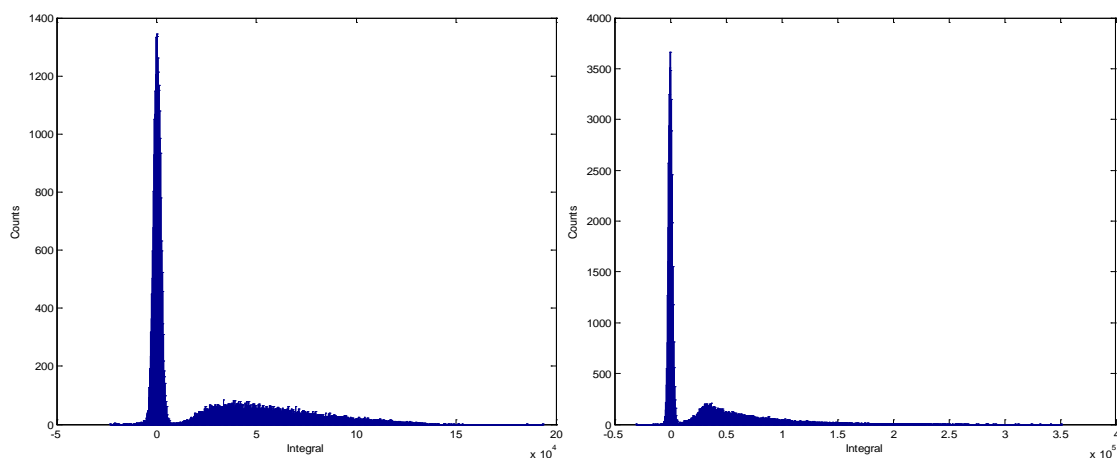


Figure 32: Histogram of legitimate and illegitimate medium pulses from a ^{137}Cs source (left) and ^{60}Co source (right)

component can be easily and accurately determined. Hence the use of a threshold works well for verifying the presence of a medium component when a slow component is absent. However, the use of a threshold to verify the presence of a slow component does not work as well. A compromise is needed.

5.4 Hybrid Fast-Slow Ratio Pulse-Fitting Method

As discussed in previous sections, both the fast-slow ratio and the pulse fitting method have weaknesses. The fast-slow ratio is unable to analyze coincident pulses, and pulses that lie outside the set boundaries are excluded. The pulse-fitting method is not a robust method for determining if a slow component is present. Counting illegitimate slow

components distorts the BC-444 spectrum by erroneously subtracting non-existent slow components. Legitimate slow pulses that are lost become part of the BC-444 spectrum. These two methods have different strengths and weaknesses, suggesting a hybrid of the two methods is optimal.

The method chosen in this work uses the fast-slow ratio method as the primary method to analyze each pulse. The fast-slow ratio method analyzes those pulses that fall within the boundaries for the three scintillation layers (Figure 33). Mixed beta-photon sources usually result in about 95% of pulses falling into one of the three regions (i.e. no coincident interactions). The pulse fitting method is the secondary method, analyzing those pulses (single event and coincident) that lie outside of the boundaries. When these two processes are coupled together, approximately 99% of the pulses are analyzed (i.e. only 1% or less are rejected due to misclassification).

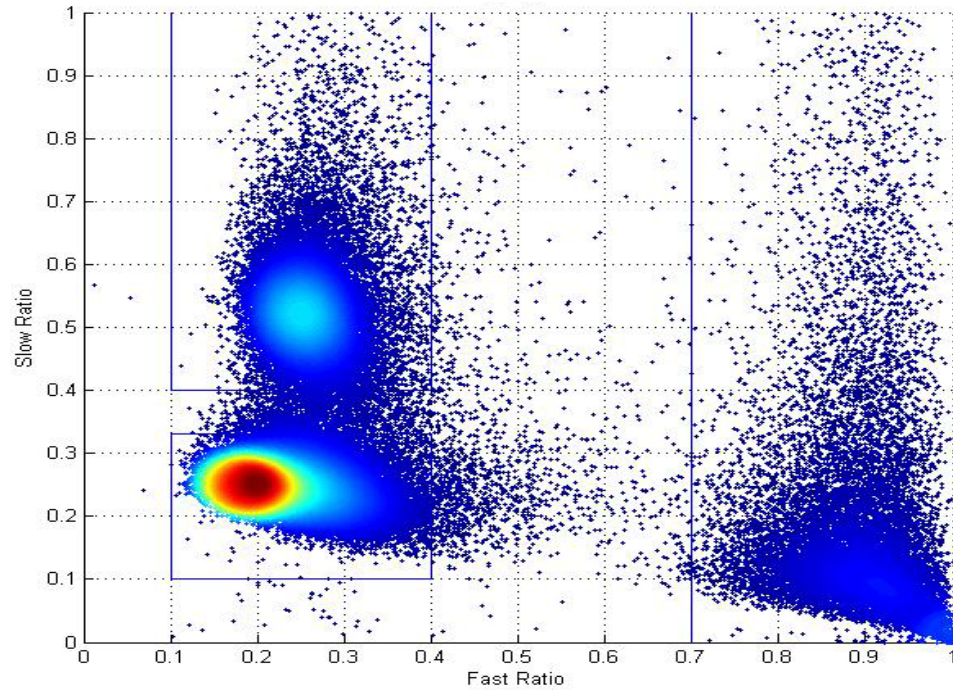


Figure 33: Two-dimensional scatter plot of fast and slow ratios for ^{137}Cs pulses; boundaries are shown

5.4.1 Determining Threshold Values

As discussed in the previous section, finding a threshold value for the area calculated using the slow fit method is complicated since there is an overlap between the legitimate and illegitimate slow pulse areas. It is possible, however, to determine a threshold value that decreases the loss of legitimate pulses and the passing of illegitimate pulses. A simple MATLAB algorithm was used to plot these percentages as a function of threshold value (Figure 34). As the threshold increases, the percent of illegitimate slow

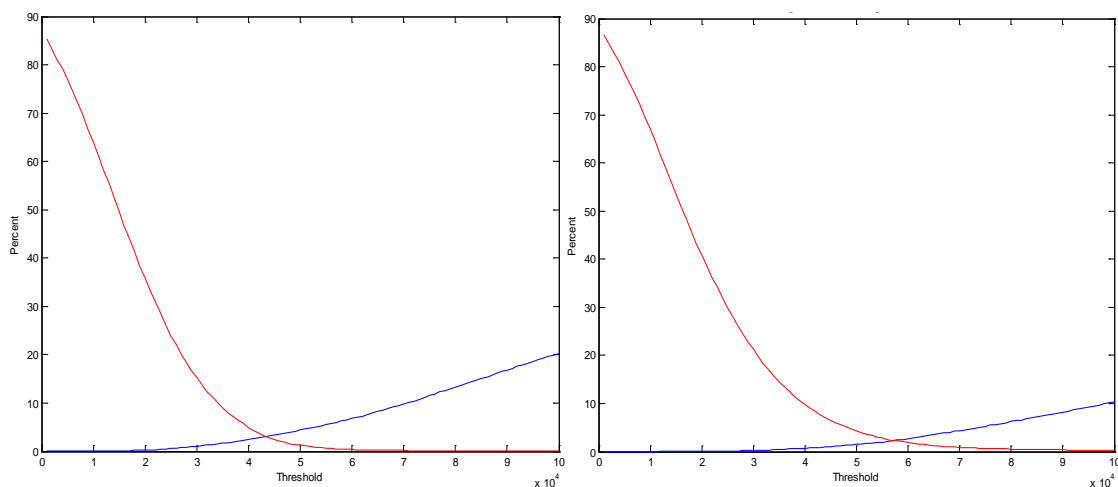


Figure 34: Percent of legitimate slow lost (blue) and illegitimate slow passed (red) as a function of threshold value for ^{137}Cs (left) and ^{60}Co (right)

components that are passed approaches zero, but the loss percentage of legitimate slow components increases. The natural choice would be to use the threshold value at the intersection of the two curves as the compromise. The point of intersection differs, however, by photon energy. As photon energy increases, the curve representing the legitimate lost shifts to higher thresholds, while the curve representing the illegitimate also shows a slight shift toward higher thresholds. For this work, the intersection threshold of the higher energy photons was chosen because it was a good compromise. For higher energy photons, the percentage of illegitimate passed and legitimate lost is low. For lower energy photons, a higher percentage of legitimate were lost, however, the percentage of illegitimate passed was extremely low. The loss was deemed acceptable because the lost legitimate pulses aren't weighted heavily (lower energy), representing only a minute difference in the measured dose.

Coincident pulses which contain both a slow and medium component require an additional threshold. When the algorithm determines that a slow component is present, it

subtracts the slow component, ideally leaving only the medium component. However, due to noise in the signal, artifacts may remain potentially incorrectly classified as a

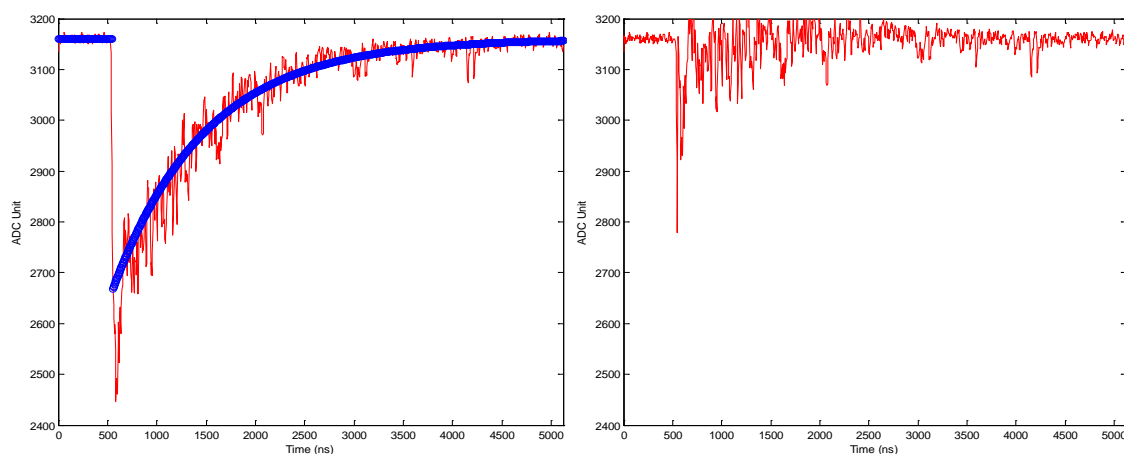


Figure 35: Remainder (right) following subtraction of slow fit from a slow pulse (left)

medium component (Figure 35). To prevent this error, a threshold must be set. To determine this threshold value, the slow component is estimated and subtracted for pulses exclusively from the slow (CaF_2) scintillation layer. The remainder is then integrated; these represent illegitimate medium components. The medium fit method was applied to legitimate and illegitimate medium components and the integrals were calculated. The percentage of legitimate medium components lost and illegitimate medium components passed was plotted as a function of threshold value (Figure 36). Once again the intersection is the natural choice for the threshold value. Once again the intersection for higher energy photons was selected as the threshold value.

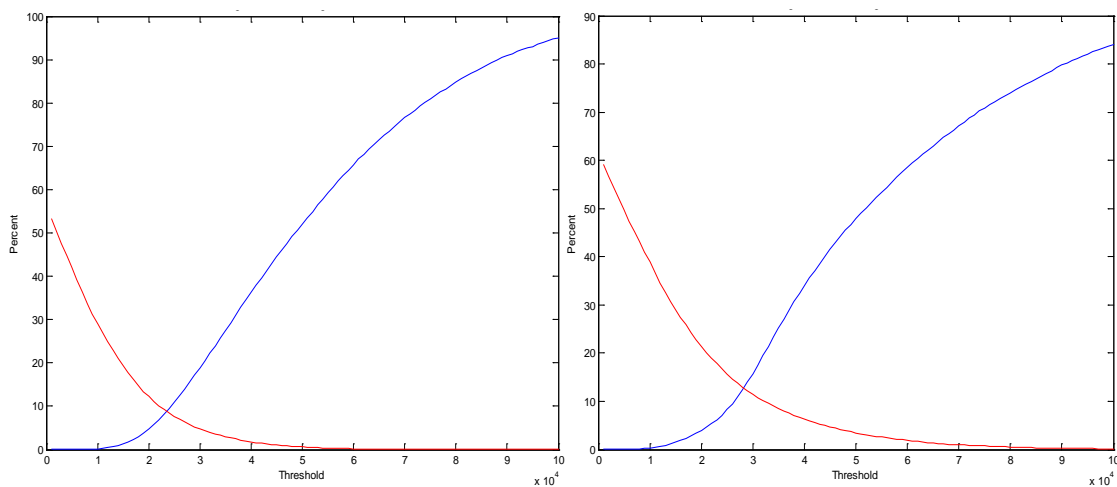


Figure 36: Percent of legitimate medium lost (blue) and illegitimate medium passed (red) as a function of threshold value for ^{137}Cs (left) and ^{60}Co (right)

5.4.2 Implementation

For the work herein, we utilized an FPGA-based digital oscilloscope design. The hardware used for the digital oscilloscope was a two-channel FPGA-based Digital Pulse Processor, DPP2.0 (Figure 37). The DPP2.0 operated at 200 MHz with a 12-bit sampling resolution Analog-to-Digital Converter (ADC). The DPP2.0 performed the digital pulse processing on the Xilinx Spartan-3 FPGA. (Alhawsawi, 2011) The FPGA-based digital oscilloscope interfaced with the host-PC through a MATLAB algorithm.



Figure 37: Two-channel digital pulse processor, DPP2.0

The pulses collected by the digital oscilloscope were analyzed by the hybrid pulse shape discrimination method illustrated in Figure 38. As described earlier, pulses are

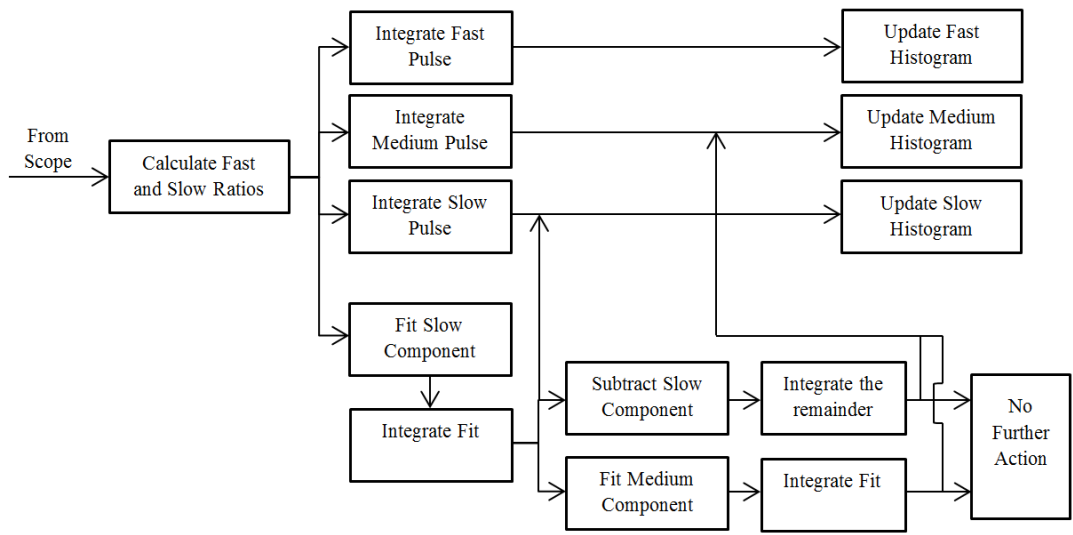


Figure 38: Hybrid fast-slow ratio pulse fitting pulse shape discrimination process

integrated for the three time intervals, T_1 , T_2 and T_3 . The fast and slow ratios are calculated using equations (17) and (18) respectively. These ratios are evaluated to see if the pulse falls in the boundaries set for a fast, medium or slow pulse. If it does not fall in

any of the three regions, a slow fit is assumed and the integral of the fit is calculated. If the integral is greater or equal to the slow pulse/component threshold, the slow pulse histogram is updated, and the slow component is subtracted. The remainder is integrated over the length of the medium pulse. If the integral satisfies the medium component threshold, the medium pulse histogram is updated, otherwise the process ends.

If the integral of the slow fit is less than the threshold, a medium fit is assumed and the integral of the fit is calculated. If the integral satisfies the medium pulse, the medium pulse histogram is updated, otherwise the process ends. After the process ends, another pulse from the oscilloscope is loaded and the entire pulse discrimination process restarts.

If the pulse is not a coincident event, the Riemann sum of the pulse is generated, not the integral of the fit. This step improves the accuracy of the measurement since the integral of the fit is merely an estimate. The integral of the fit is recorded to the spectrum only when it is part of a coincident pulse.

5.4.3 Limitations

The above process involves a VHDL algorithm for the digital oscilloscope and a MATLAB algorithm for the pulse shape discrimination and energy spectrum. The VHDL algorithm does not have a live-time counter so there is no direct method to determine the actual live time. This shortcoming is discussed in section 7.3.

In section 5.4.2 the methods of choosing threshold values for the slow component and the medium component following the removal of the slow component were

discussed. A clear separation between areas for legitimate and illegitimate components did not exist, so a good threshold is not possible. Hence a compromise was needed, resulting in slow pulses being lost from the slow (CaF_2) spectrum while distorting the medium (BC-444) spectrum. These errors, however, are minor since the estimated occurrence is small, a fraction of a percent.

The above method is unable to measure the fast component of a coincident pulse involving the fast (BC-400) layer. When a medium or slow component has been identified, it is subtracted. However, the remainder (Figure 35) makes it difficult to determine whether or not a fast component is truly present. Therefore, no effort is made to measure the fast component of a coincident pulse.

6 DOSIMETER CALIBRATION

6.1 Introduction

From previous discussions, the integral of a signal pulse is proportional to the absorbed energy in a scintillator. Calibration relates that integral to energy deposition through use of a proportionality (calibration) factor. The endpoint of the calibration will be to characterize the time-integrated energy deposition spectrum for the ultimate calculation of absorbed dose. The dosimeter calibration is one of most important parts of this work, and a considerable amount time was spent ensuring that calibrations were as accurate as possible. Since absorbed dose is defined as the energy deposited per unit mass, errors in the calibration will result in more uncertainty in the dose measurements.

The calibration is performed by collecting a raw spectrum for each scintillation layer. Spectral features (e.g. full-energy peak, Compton edge, etc.) that correlate to known energies are used as calibration points to determine the integrated signal-to-energy relationship. The type of radioactive source used for the calibration of a scintillator is important. Sources that emit photons are preferred over betas because photons are mono-energetic whereas beta particles have a continuous energy spectrum. Moreover, spectral features that are used for calibration (e.g. full-energy peak and Compton edge) result from photon interactions. At least three features are required for the calibration. Since there is a strong linearity between absorbed energy and scintillation light intensity, the calibration should be linear with energy.

6.2 CaF₂ Layer Calibration

Calcium fluoride is the third layer, and is centered at a density thickness of 1000 mg cm⁻². At this depth electrons emitted from a calibration source possesses insufficient energy to penetrate, thus mono-energetic photons are used to calibrate that scintillation layer. Calibration of the CaF₂ layer was performed using ¹³⁷Cs, ²²Na and ¹³³Ba sources (Figure 39). Since this layer is very thin, 0.6 mm, the majority of the interactions are Compton events. The Compton edge in each spectrum can be used as a calibration point.

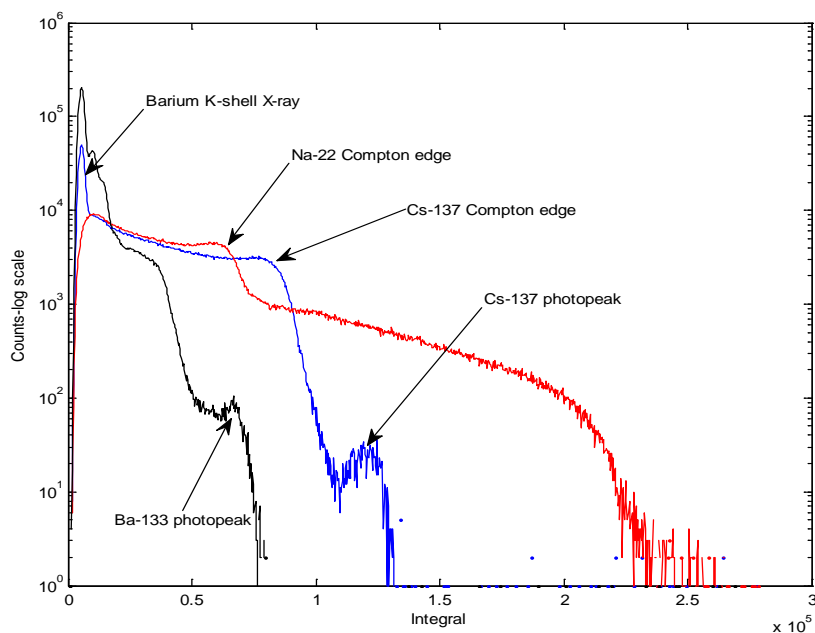


Figure 39: CaF₂ layer spectra of ¹³⁷Cs (blue), ²²Na (red), and ¹³³Ba (black)

However, the precise location of the edge is somewhat difficult to determine because of its rounded shape. This occurs because the orbital electrons are not unbound or free. The site of the Compton edge was chosen to be the intersection of two lines extending from the regions of the continuum that flank the edge.

Full-energy deposition occurs for low-energy photons as evidenced by the barium K-shell X-ray peak in the ^{137}Cs spectrum. Because this scintillation layer is very thin, full-energy deposition for higher energy photons occurs with a much lower probability as evidenced by the ^{137}Cs 662 keV and ^{133}Ba 356 keV full-energy peaks. The spectral features used for the calibration are displayed in Table 6. A linear fit was applied to the calibration points (Figure 40). The calibration equation is included in the figure.

Table 6: Spectral features used in the calibration of the CaF_2 layer

Spectra Feature	Integral	Energy (keV)
Zero	0	0
Barium K-shell X-ray	5325.325	32
^{22}Na Compton edge	61381.38	340
^{133}Ba photopeak	66706.71	356
^{137}Cs Compton edge	85485.49	480
^{137}Cs photopeak	119119.1	662

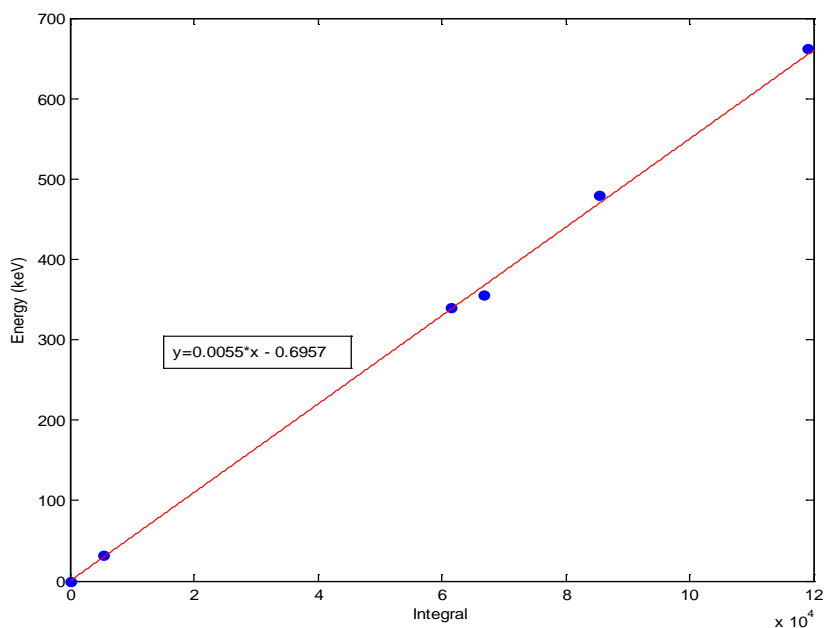


Figure 40: Calibration curve for the CaF_2 layer

6.3 BC-444 Layer Calibration

BC-444 is the second layer, and is centered at a density thickness of 300 mg cm^{-2} . At this depth electrons emitted from a calibration source may penetrate and interact with this scintillator. To avoid this, electrons were shielded using a thin copper absorber, approximately 0.5 mm. Calibration of the BC-444 layer was performed using a ^{60}Co and ^{133}Ba source (Figure 41). Since this layer is also very thin, 0.6 mm, virtually all of the

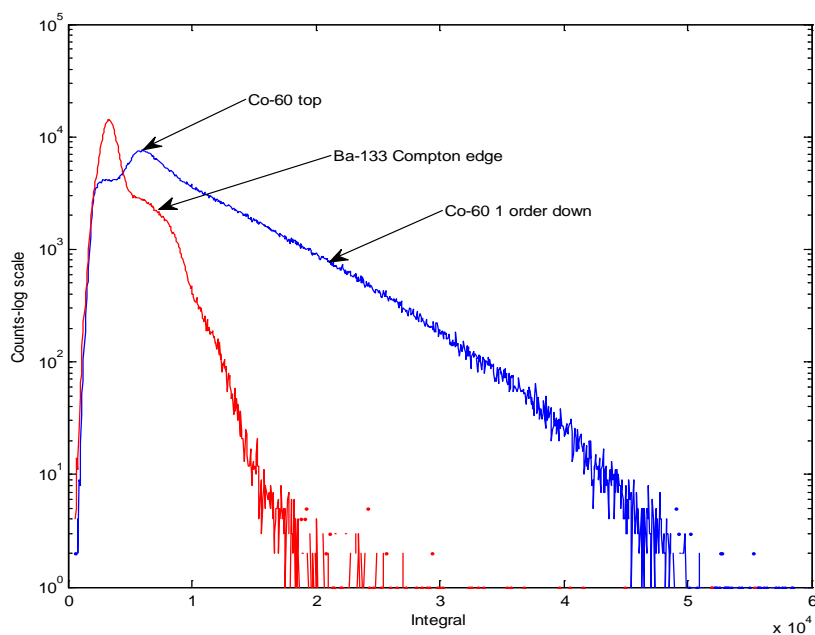


Figure 41: BC-444 spectra of ^{60}Co (blue) and ^{133}Ba (red)

interactions are Compton scattering. Spectra from this scintillation layer lack sufficient features for calibration, so an alternate method is required. Cazalas (Cazalas, 2009) encountered the same issue when attempting to calibrate a similar plastic scintillator. He used an approach based on a method developed by Siciliano. (Siciliano et al., 2008) Calibration points are extracted from experimental spectra by comparing them to energy

spectra from Monte Carlo simulations of the dosimeter. Similar spectral features, such as the Compton edge and maxima are used to reference bins from the experimental spectra

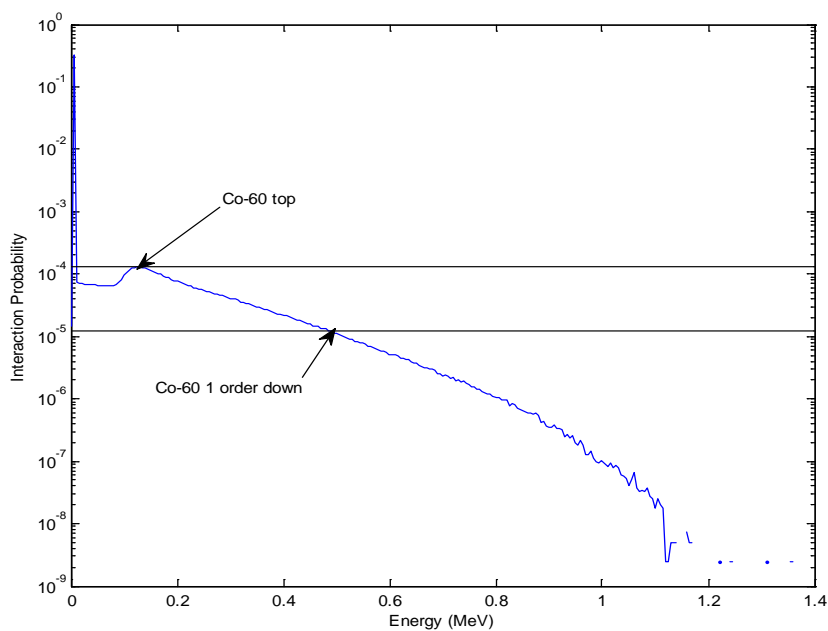


Figure 42: MCNP5 ^{60}Co energy spectrum for the BC-444 layer

to energies from the Monte Carlo spectra. The features that Cazalas used in the comparisons were the Compton maximum, as well as the location one order of magnitude below this maximum. This method is applied to the ^{60}Co deposition spectrum (Figure 42). The calibration points are displayed in Table 7. The calibration curve is shown in Figure 43.

Table 7: Spectral features used in the calibration of the BC-444 layer

Spectra Feature	Integral	Energy (keV)
Zero	0	0
⁶⁰ Co top	6006.006	125
¹³³ Ba Compton edge	7867.868	186
⁶⁰ Co 1 order down	21141.14	485

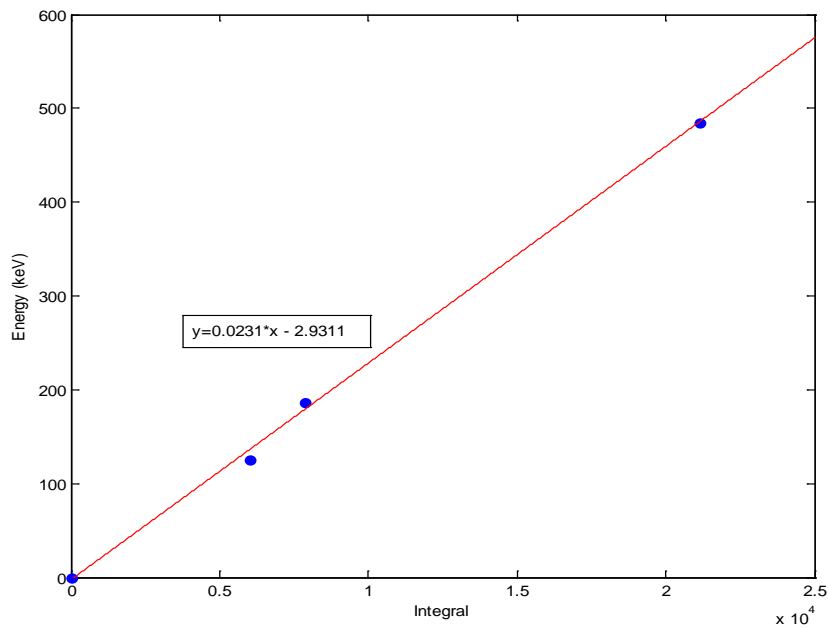


Figure 43: Calibration curve for the BC-444 layer

6.4 BC-400 Layer Calibration

BC-400 is the first layer, and is centered at a density thickness of 7 mg cm^{-2} . At this depth electrons emitted from a calibration source will penetrate and interact with the scintillator. To avoid this, electrons were shielded using a thin copper absorber, approximately 0.5 mm. Since this layer is extremely thin, $20 \text{ }\mu\text{m}$, the vast majority of interactions are Compton scattering. The method used for the second (Bc-444) layer does not work for this layer as shown by Cazalas. (Cazalas, 2009) For low-energy photons, approximately 30 keV or lower, there is a probability of photoelectric interactions with

the base material of the scintillator (Figure 1). If photoelectric interactions occur with a sufficient probability, the spectrum should have a full-energy peak centered at the photon energy. The approach used in the current work attempts to use full-energy peaks of low-energy photons from ^{137}Cs (32 keV) and ^{241}Am (60 keV and 26 keV) for determining calibration points (Figure 44). At 60 keV, Compton interactions dominate in the BC-400 scintillator. Therefore a full-energy peak at 60 keV is not expected. There is uncertainty

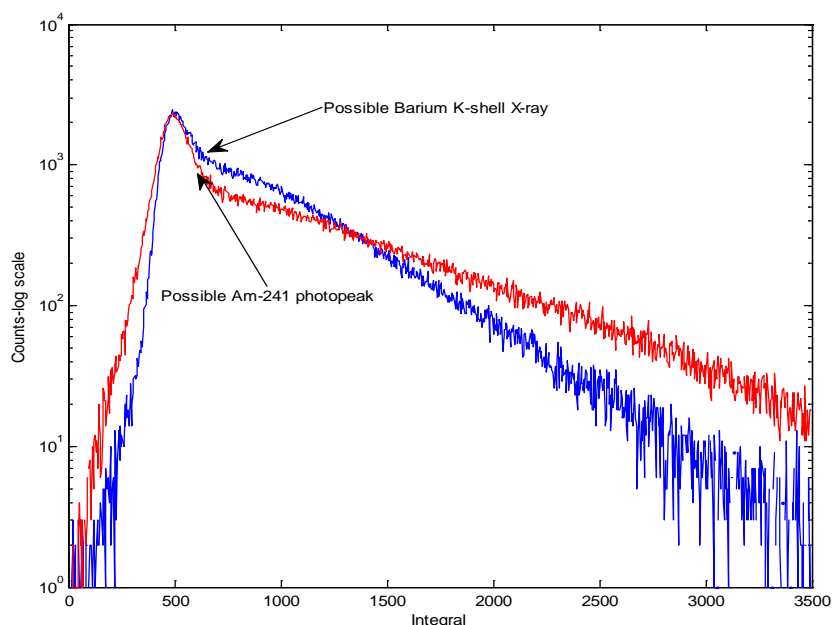


Figure 44: BC-400 spectra of ^{137}Cs (blue) and ^{241}Am (red)

whether this approach would provide the needed calibration points. The peak in the ^{241}Am spectrum is most likely the 26 keV gamma-ray because its centroid is slightly offset to the left from the ^{137}Cs 32 keV peak. Therefore the energy must be lower, ruling out the ^{241}Am 60 keV gamma-ray. There are an insufficient number of reliable calibration points to confidently identify a single calibration equation. With two calibration points

(Table 8), three possible calibration equations can be formed (Figure 45). The calibration results suggest that the approach used does not work. It is believed that the energies are too high for photoelectric events to occur with a reasonable probability. Another possibility is that the scintillator is too thin, allowing photoelectrons to escape the scintillation layer before depositing all of their energy.

Table 8: Possible spectral features used in the calibration of the BC-400 layer

Spectra Feature	Integral	Energy (keV)
Zero	0	0
²⁴¹ Am photopeak	472.973	26
Barium K-shell X-ray	490.4905	32

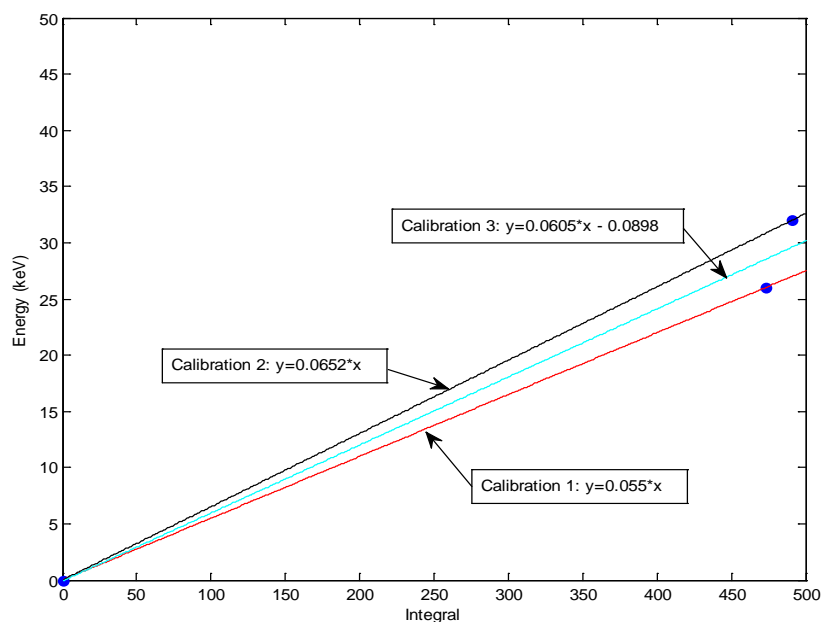


Figure 45: Possible calibration curves for the BC-400 layer

7 RESULTS AND DISCUSSION

7.1 Calibration Sources

The sources used for the dose measurements are 1 inch plastic disk sources manufactured by Spectrum Techniques. The source material is deposited as a liquid in the cavity, approximately 5 μL , and allowed to dry. When dried, it forms an area between 3 and 5 mm in diameter. Epoxy is then used to seal the cavity. The source casing is made of stock Plexiglas, 3 mm thick. The window thickness is 0.015 inches. (Stevens, 2013) The radionuclides used and the nominal activities are listed in Table 9. The nuclides used in this study emit a broad range of photon energies (88 keV to 1332 keV). The exact dates of calibration are not available, requiring estimations for the amount of time since calibration, but uncertainties related to source activity are shown to be insignificant.

Table 9: Approximate activities of the sources used for dose measurements

Radionuclide	Radiation Type	Half-life (d)	Initial Activity (μCi)	Calibration Date	Date of Measurement	Corrected Activity (μCi)
^{109}Cd	Gamma	463	1	02/2012	06/2013	0.48 ± 0.01
^{137}Cs	Gamma, Beta	10976	1	12/2011	06/2013	0.97 ± 0.0009
^{60}Co	Gamma, Beta	1925	1	02/2012	06/2013	0.84 ± 0.005
^{22}Na	Gamma, Positron	950	1	02/2012	06/2013	0.70 ± 0.008

7.2 Monte Carlo Dose Rate Calculation Method

Measured dose rates were compared to Monte Carlo dose rate calculations using MCNP5 simulations. Monte Carlo dose rates were calculated using the *F8 tally option and multiplying the output by the source activity, and dividing by the scintillator mass.

The MCNP5 geometry was composed of a tissue cylinder, 20 cm in diameter and 11 cm thick. The simulated dose volumes were 10 cm^2 cylinders 20 μm thick, thick enough to ensure statistical soundness. (Sherbini, 2008) The source was modeled as an infinitely thin 4 mm diameter disk.

7.3 Measurement of Dose Rate

The measured dose rates were obtained from energy spectra collected for each of the three scintillation layers. The total absorbed energy was obtained by multiplying a pulse height distribution (Figure 46) by the energy (Figure 47), and summing the bins. The total energy was divided by the scintillator mass to obtain the dose, and then divided by the detection live time to obtain dose rate.

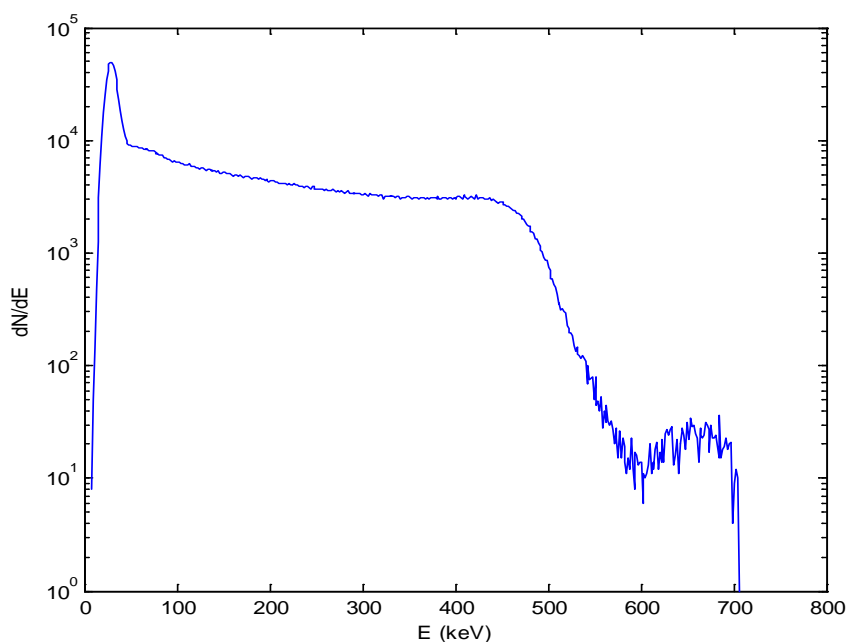


Figure 46: The pulse height distribution from the CaF_2 scintillation layer of a ^{137}Cs source

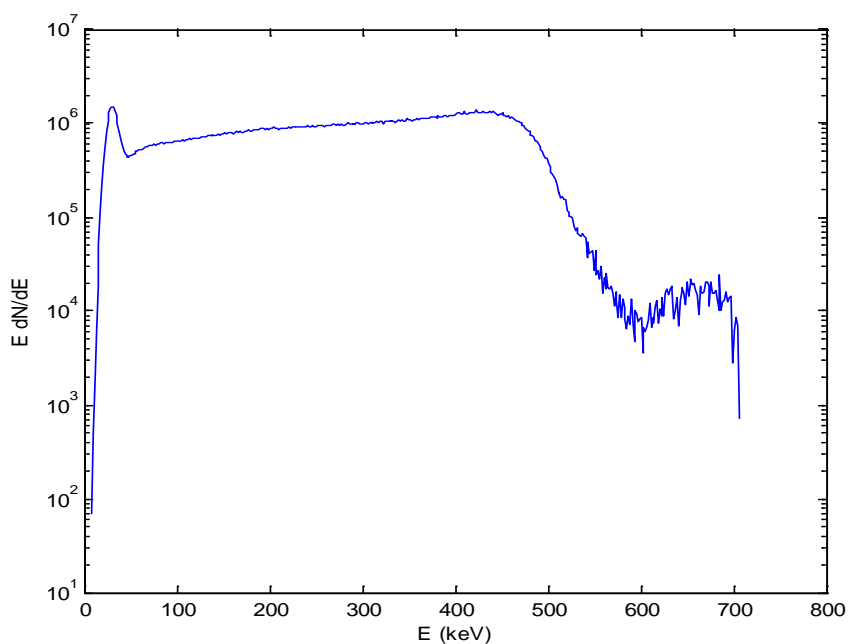


Figure 47: Multiplication of the pulse height distribution in Figure 46 by the energy

As discussed in Section 5.4.3, a direct method to calculate the live time wasn't available, so the live time had to be measured. Live time is the difference between real time and total system dead time. The system dead time, τ , is assumed to be constant and occurs for each true event taking place during the live time. True events which occur during the system dead time are lost.

The system dead time was estimated using the two-source method. This method utilizes two radioactive sources, each offering a high count rate to the detector. Count rates are determined with one source (m_1), with the other source (m_2), with both sources (m_{12}), and with neither source (m_b). The following set of equations is then used to calculate system dead time per detection event (Knoll, 2010):

$$\tau = \frac{X(1 - \sqrt{1 - Z})}{Y} \quad (26)$$

where $X \equiv m_1 m_2 - m_b m_{12}$ (27)

$$Y \equiv m_1 m_2 (m_{12} + m_b) - m_b m_{12} (m_1 + m_2) \quad (28)$$

$$Z \equiv \frac{Y(m_1 + m_2 - m_{12} + m_b)}{X^2}. \quad (29)$$

The system dead time was calculated using a ^{90}Sr split source (Table 10). At more than 3 milliseconds, the measured system dead time is very large in comparison to other detectors.

Table 10: Dead time measurement using the two-source method

m_1 (cps)	m_2 (cps)	m_{12} (cps)	m_b (cps)	τ (ms)
207 ± 0.293	213 ± 0.359	254 ± 0.301	3.9 ± 0.00468	3.1 ± 0.0532

It is believed that the large dead time is primarily due to the digital oscilloscope's dependence on MATLAB. To a lesser degree, the pulse shape discrimination and energy-spectrum collection contribute to the total dead time. It is expected that, if the digital oscilloscope, pulse shape discrimination and energy spectrum were integrated on a FPGA, the dead time would be greatly reduced. The total system dead time is determined by multiplying τ by the number of pulses counted. The real time was calculated using an internal MATLAB clock. With the real and total system dead time the live time can be obtained. Despite this method, there are still concerns about the accuracy of the live time. An FPGA system would measure the live time accurately by updating a counter whenever it is measuring pulses. Improvement in the live time measurement will undoubtedly affect the accuracy of the measured dose.

The long dead time places a restriction on the count rate of the system. A maximum count rate of approximately 250 cps was observed for the sources listed in Table 9. The maximum count rate was confirmed by measuring a 100 mCi ^{241}Am source. The small maximum count rate is disadvantageous because it will require longer counting times for sources. Unless the source is short-lived, the maximum count rate is not expected to affect measured doses.

7.4 Error Analysis

The dose-estimate uncertainty is calculated by making reasonable assumptions, and utilizing established error propagation and analysis techniques. Assumptions were made for the uncertainty in energy calibration, radioactive source strength, and scintillator mass. Monte Carlo simulation standard error was kept below 5% by running a sufficient number of particle histories. VARSKIN 5 does not calculate the uncertainty in its estimates, therefore none are included.

Appreciable dead time losses have been shown to distort counting statistics away from true Poisson behavior (Müller, 1973). If the total dead time is greater than about 20%, these distortions may become significant. Although the total system dead time in this work exceeds 20%, the implication is simply that our estimates of counting uncertainty do not follow Poisson statistics. Uncertainties shown in the current work, however, were calculated assuming Poisson behavior with the caveat that expected statistical fluctuations may not be modeled exactly. Future implementation of this system

on an FPGA will greatly decrease the total system dead time (we estimate below 10%) and the uncertainty estimates will again follow expected variation. (Knoll, 2010)

7.5 Dose Rate to Deep Tissue

The calcium fluoride layer is meant to estimate the dose to the deep layer (1000 mg cm⁻²). Measured dose rates were compared to dose rates calculated with MCNP5 and VARSKIN 5. The dose rate comparisons are summarized in Table 11. The label *MCNP skin* is the Monte Carlo simulation of tissue layers. Measured dose rates tended to

Table 11: Dose rate comparisons for deep tissue

Radionuclide	Measured (nGy.s ⁻¹)	MCNP5 Skin (nGy.s ⁻¹)	VARSKIN 5 (nGy.s ⁻¹)
¹⁰⁹ Cd	0.22 ± 0.0040	0.470 ± 0.0196	0.32
⁶⁰ Co	8.4 ± 0.48	6.56 ± 0.113	12.0
¹³⁷ Cs	3.4 ± 0.10	4.10 ± 0.0907	3.54
²² Na	10 ± 0.75	10.3 ± 0.147	9.04

underestimate the dose rate for lower energy photons. Conversely, dose rates appear to be overestimated at higher energies. The only exception was the VARSKIN 5 calculation for ⁶⁰Co which exceeded the measured rate by 50%. Measured dose rates for the deep layer agree fairly well with MCNP5 and VARSKIN 5 calculations. Generally, measured dose rates are within 30% of MCNP5 and VARSKIN 5 calculations. The measured dose rates may be more accurate and agree better with the standard dose calculation methods if the exact live time was known. This layer is suitable for estimating the deep dose.

The calcium fluoride scintillation layer, used to estimate absorbed dose to the deep layer is not tissue-equivalent, differing in elemental composition and density. Therefore, that scintillation layer is not necessarily representative of tissue in terms of

interactions with radiation. Absorbed dose to the CaF_2 scintillator can be related to tissue dose by ratios of the mass-energy absorption coefficients and collisional mass stopping powers,

$$D_{t,photon} = D_{\text{CaF}_2,photon} \left(\frac{\mu_{en}}{\rho} \right)_{\text{CaF}_2}^{tissue} \quad (30)$$

$$D_{t,electron} = D_{\text{CaF}_2,electron} \left(\frac{S}{\rho} \right)_{\text{CaF}_2}^{tissue} \quad (31)$$

where $\frac{\mu_{en}}{\rho}$ is the mass-energy absorption coefficient, D_{photon} is the absorbed dose from photons, $D_{electron}$ is the absorbed dose from electrons, and $\frac{S}{\rho}$ is the collisional mass stopping power. Ratios of the mass-energy absorption coefficients and collisional mass stopping powers as a function of energy are shown in Figures 48 and 49, respectively. The application of equations 30 and 31 is not possible because current methods are unable to determine the dose contributions specifically from electrons or photons. In addition, the mass stopping power is dependent on the electron energy spectrum, which the current system is also unable to determine.

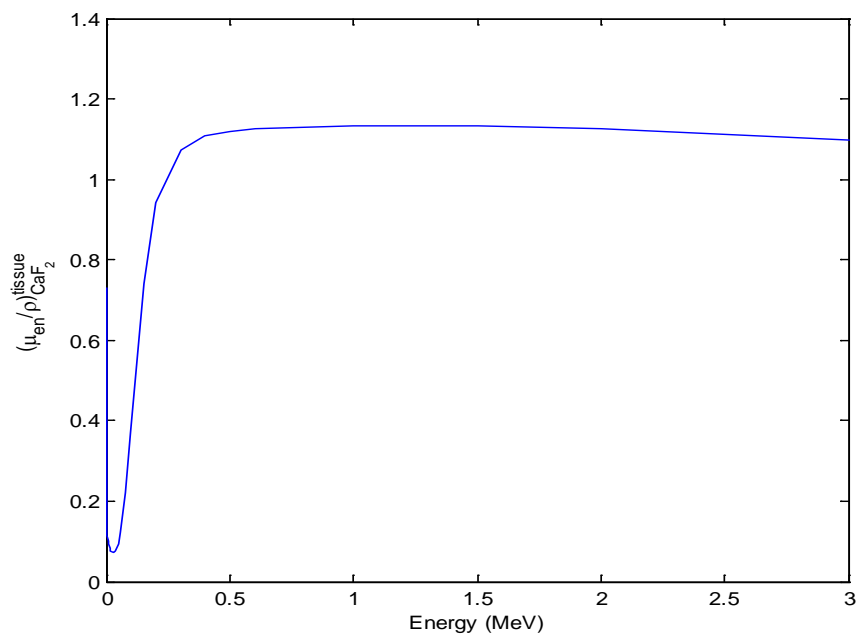


Figure 48: Ratios of the mass-energy absorption coefficient for tissue and calcium fluoride as a function of energy (taken from NIST, 1996)

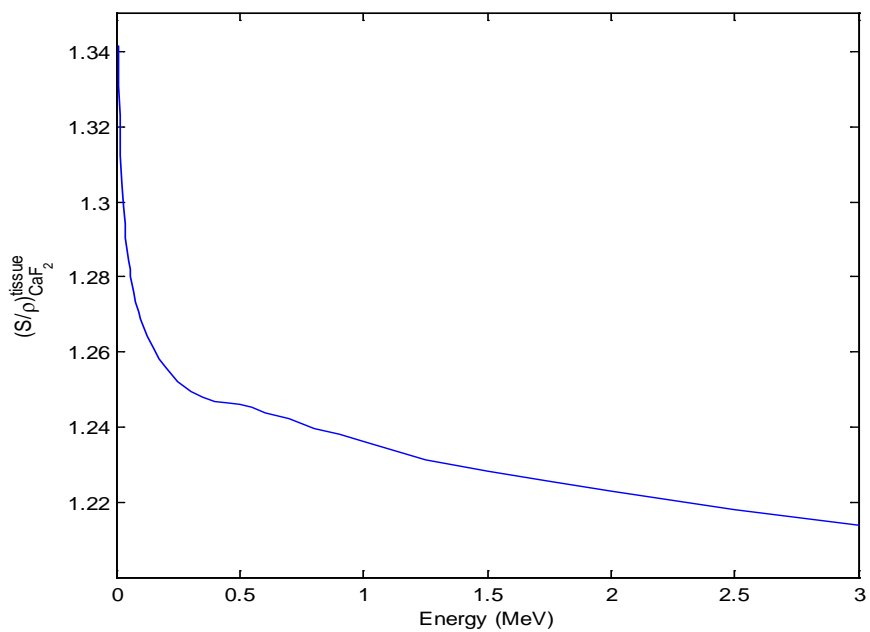


Figure 49: Ratios of the mass stopping power for tissue and calcium fluoride as a function of energy (taken from NIST, 1998)

7.6 Dose Rate to Lens of the Eye

The BC-444 layer is available to estimate the dose to the lens of the eye (300 mg cm⁻²). Measured dose rates at this depth were compared to dose rates calculated with MCNP5 and VARSKIN 5. The dose rate comparisons are summarized in Table 12.

Table 12: Dose rate comparisons for eye-lens dose

Radionuclide	Measured (nGy.s ⁻¹)	MCNP5 Skin (nGy.s ⁻¹)	VARSKIN 5 (nGy.s ⁻¹)
¹⁰⁹ Cd	0.61 ± 0.010	1.43 ± 0.0431	1.25
⁶⁰ Co	20 ± 1.2	16.1 ± 0.202	31.3
¹³⁷ Cs	7.3 ± 0.22	10.4 ± 0.149	9.37
²² Na	24 ± 1.7	25.3 ± 0.318	23.7

The trend of the measured dose rates to underestimate at low energies but overestimate at higher energies was also observed, except for one case. The ⁶⁰Co measured dose rate is lower than the VARSKIN 5 calculated dose rate, and higher than the MCNP5 calculated dose rate. The cause for the trend is unknown. Measured dose rates are within a factor of two of either Monte Carlo or VARSKIN 5 calculations. Generally, measured dose rates are within 30% of MCNP5 and VARSKIN 5 calculations. This layer is deemed suitable for estimating the eye dose.

7.7 Dose Rate to Shallow Tissue

The BC-400 layer is used to estimate the dose to the shallow layer of skin (7 mg cm⁻²). Measured dose rates were compared to dose rates calculated with MCNP5 and VARSKIN 5. As discussed in Section 6.2, there are three possible calibration equations that could reasonably be obtained given the sparse mechanistic calibration features. The

dose rate comparisons with the results of MCNP and VARSKIN, therefore, for each calibration equation are provided in Table 13.

Table 13: Dose rate measurements of shallow dose using calibration equations 1 through 3

Radionuclide	Measured 1 (nGy.s ⁻¹)	Measured 2 (nGy.s ⁻¹)	Measured 3 (nGy.s ⁻¹)	MCNP5 Skin (nGy.s ⁻¹)	VARSKIN 5 (nGy.s ⁻¹)
¹⁰⁹ Cd	5.8 ± 0.32	6.9 ± 0.37	6.4 ± 0.35	3.55 ± 0.0919	5.14
⁶⁰ Co	130 ± 9.8	150 ± 12	140 ± 11	42.5 ± 0.334	45.2
¹³⁷ Cs	50 ± 2.9	60 ± 3.5	55 ± 3.2	260 ± 0.391	274
²² Na	120 ± 10	140 ± 12	130 ± 11	263 ± 2.89	176

Measured dose rate comparisons with MCNP5 and VARSKIN 5 suggest that possibly all of the calibration equations are invalid. It was intended that the calibration approach for this scintillator use full-energy peaks from interactions of low-energy photons for calibration points. Since the calibration equations appear to be invalid, it can be assumed that the peaks in the ²⁴¹Am and ¹³⁷Cs spectra are not full-energy peaks. It is probable that photoelectric events did indeed occur. The photoelectrons created could have escaped the extremely thin scintillator without having deposited all of their kinetic energy; hence the absence of a typical full-energy peak. If the BC-400 scintillator is thicker, the photoelectrons may deposit all of their energy, leading to full-energy peaks needed for the calibration. While results are encouraging for the shallow dose layer, the calibration of the BC-400 scintillator at this point is merely a guess. As such these dose estimates should be used with caution.

8. CONCLUSION AND FUTURE WORK

The triple-layer phoswich dosimeter design is a novel approach to executing simultaneous depth-dose measurements for radiation contamination of the skin. Scintillators with large difference in decay time are situated between tissue-equivalent absorbers, allowing dose estimation for the shallow (7 mg.cm^{-2}), lens (300 mg.cm^{-2}), and deep (1000 mg.cm^{-2}) depths. Pulse shape discrimination is a difficult task, requiring a hybrid of the fast-slow ratio and pulse fitting methods. The pulse shape discrimination worked exceptionally well.

Generally, dose measurements agree well with either MCNP5 or VARSKIN 5 for dose estimates to the deep and lens layers of tissue. A pattern for the measured dose rates was identified for the CaF_2 (deep) and BC-444 (lens) scintillation layers. Measurements tended to underestimate the dose rate for lower energies and overestimate the dose rate for higher energies.

The BC-400 (shallow) layer, however, was problematic. A valid energy calibration could not be performed for the first layer due to the lack of reliable spectral features. Inability to calibrate this scintillator is thought to be due, in part, to the thinness of the scintillator and low probability of full-energy deposition. Further work is needed to calibrate and possibly redesign the scintillation layer with a thicker scintillator.

A slight modification to the pulse shape discrimination approach should be implemented in future work. Currently, BC-400 (fast) pulses are only identified with the fast-slow ratio portion of the pulse shape discrimination process. Therefore, fast pulses

which lie outside of the boundaries are discarded. In the current work, these losses are minimal and have little practical effect since the vast majority of BC-400 pulses are identified by the fast-slow ratio method. Fast pulses that are not identified by the fast-slow ratio method can be identified by the pulse-fitting method. A pulse that is not identified as containing a slow or medium component should be identified as a fast pulse. A better method to differentiate whether a slow component or pulse is present, other than applying a simple threshold, is needed to avoid the loss of legitimate slow pulses, and the distortion of the eye-dose spectrum. The accuracy of the pulse shape discrimination process used herein would be increased with improvements in the pulse waveforms. These waveform improvements are directly correlated to light collection. Future efforts should be made to develop a more efficient light guide and to enhance clarity of, and transmission through, the absorbers.

The current setup, involving MATLAB, requires long counting times due to the low detection efficiency and large system dead time. The large system dead time complicates estimation of counting error. In addition, the current system does not have the ability to measure the live time directly. Future work will implement the oscilloscope, pulse shape discrimination and energy spectrum processes on an FPGA. This will allow real-time measurements with system dead time improvements of approximately three orders of magnitude or greater, greatly improving Poisson statistics. The live time can easily and accurately be determined through implementation of a digital counter.

The end product will not need to interface with a host computer. The dosimeter will be portable, containing an internal battery instead of relying on external power supplies. The first objective will be met by developing a VHDL code that performs the oscilloscope, pulse shape discrimination and energy spectrum on a FPGA-based digital pulse processor. This code will most likely require three different two-port block rams. The implementation of all three processes on an FPGA will decrease the amount of dead time, requiring less time to gather a sufficient number of counts to obtain a dose rate measurement that has an acceptable uncertainty. The second objective will require a substantial amount of electrical engineering. The high voltage requirement of the PMT can be achieved by implementing a low-to-high voltage converter. The size of the dosimeter body needs to be reduced. A smaller dosimeter body was designed and built in this work, but a more efficient light guide needs to be developed for that body design to be useful.

BIBLIOGRAPHY

- 23396, 5. F. (1991). *10CFR20: Standards for protection against radiation*. Nuclear Regulatory Commission. Office of Federal Register.
- Alhawsawi, A. M. (2011). *Study of Compton suppression capability in a triple-layer phoswich detector*. (Unpublished master's thesis). Oregon State University, Corvallis, Or.
- Attix, F. H. (1986). *Introduction to radiological physics and radiation dosimetry*. New York, NY: John Wiley & Sons.
- Aydarous, A. S., Darley, P. J., & Charles, M. W. (2004). Development of an ICCD-scintillator system for measurement of spatial dose distributions around 'hot particles'. *Radiation Protection Dosimetry*, 108(4), 317-326.
- Bingo, K., Suga, S. I., Kajimoto, Y., & Numakunai, T. (1979). Beta-ray survey meter for measuring absorbed dose rate independently of beta-ray energy. *Health Physics*, 39(1), 21-28.
- Cazalas, E. J. (2009). *Design, construction, and analysis of a skin contamination dosimeter*. (Unpublished master's thesis). Oregon State University, Corvallis, Or.
- Cember, H. (2009). *Introduction to Health Physics* (4th ed.). New York, NY: McGraw-Hill Medical.
- Cross, W. G., Wong, P. Y., & Freedman, N. O. (1991). Dose distributions for electrons and beta rays incident normally on water. *Radiation Protection Dosimetry*, 35(2), 77-91.
- Cross, W. G., Freedman, N. O., & Wong, P. Y. (1992). Beta ray dose distributions from skin contamination. *Radiation Protection Dosimetry*, 40(3), 149-168.
- Durham, J. S., Merwin, S. E., & Swinth, K. L. (1991). Skin dose evaluations using exoelectron dosimeters. *Radiation Protection Dosimetry*, 39(1-3), 67-70.
- Evans, R. D. (1955). *The atomic nucleus*. New York, NY: McGraw-Hill.
- Farsoni, A. T. (2007). *Simultaneous beta/gamma digital spectroscopy*. (Unpublished doctoral dissertation). Oregon State University, Corvallis, Or.
- Farsoni, A. T., Alemayehu, B., Alhawsawi, A., & Becker, E. M. (2012). Real-time pulse shape discrimination and radioxenon measurement in field-programmable gate array. *2012 Monitoring Research Review: Ground-Based Nuclear Explosion Monitoring Technologies*, 34. Retrieved from <http://www.rdss.info/librarybox/mrr/MRR2012/PAPERS/05-03.PDF>

- Forsythe, J. S., & Hill, D. J. T. (2000). The radiation chemistry of fluoropolymers. *Progress in Polymer Science*, 25(1), 101-136.
- Hajnal, F. (1986). Measurement of beta spectra and dose in mixed beta-photon fields. *Radiation Protection Dosimetry*, 14(2), 175-178.
- Hall, E. J. (2012). *Radiobiology for the radiologist* (7th ed.). Philadelphia, PA: Lippincott Williams & Wilkins.
- Hamamatsu Photonics. (2006). *Photomultiplier tubes: Basics and applications* (3rd ed.). Retrieved from http://www.hamamatsu.com/resources/pdf/etd/PMT_handbook_v3aE.pdf
- Hecht, E. (1987). *Optics* (2nd ed.). Reading, MA: Addison-Wesley Publishing.
- National Institute of Standards and Technology. (1996). *Tables of X-ray mass attenuation coefficients and mass energy-absorption coefficients from 1 keV to 20 MeV for elements Z=1 to 92 and 48 additional substances of dosimetric interest* [Data File]. Retrieved from <http://www.nist.gov/pml/data/xraycoef/>
- National Institute of Standards and Technology. (1998). *Stopping-power and range tables for electrons, protons, and helium ions* [Data File]. Retrieved from <http://www.nist.gov/pml/data/star/index.cfm>
- Johnson, L. O., Alvarez, J. L., Hoggan, J. M., & Dickson, R. L. (1983). Pulse shape discrimination in a portable beta-gamma dose rate meter. *IEEE Transactions on Nuclear Science*, 30(1), 543-546.
- Knoll, G. F. (2010). *Radiation Detection and Measurement* (4th ed.). Hoboken, NJ: John Wiley & Sons.
- Kriss, A. A. (2004). *A beta dosimeter and spectrometer utilizing plastic scintillators and a large-area avalanche photodiode*. (Unpublished doctoral dissertation). Oregon State University, Corvallis, Or.
- Lilley, J. S. (2001). *Nuclear physics: Principles and applications*. West Sussex, UK: John Wiley & Sons.
- Loevinger, R., Trott, N. G. (1966). Design and operation of an extrapolation chamber with removable electrodes. *The International Journal of Applied Radiation and Isotopes*, 17(2), 103-104.
- Martin, J. E. (2006). *Physics for radiation protection: A handbook* (2nd ed.). Weinheim, DE: Wiley-VCH.
- Martz, D. E., Rich, B. L., & Johnson, L. O. (1986). A portable beta spectrometer for tissue dose measurement. *Radiation Protection Dosimetry*, 14(2), 183-186.

- McWilliams, F. F., Scannell, M. J., Soares, C. G., Coursey, B. M., & Chabot, G. E. (1992). Hot particle dosimetry using Co-60 spheres. *Radiation Protection Dosimetry*, 40(4), 223-234.
- Müller, J. W. (1973). Dead-time problems. *Nuclear Instruments and Methods*, 112(1-2), 47-57.
- Setzkorn, R., Magnac, Y., Prevost, H., Nadai, J. P., Albert, L., Dusseau, L., & Fesquet, J. (1997). Hot particle dosimetry using laser heated thermoluminescent dosimetric foils compared to EGS4-PRESTA calculations. *Radiation Protection Dosimetry*, 72(2), 119-126.
- Sherbini, S., DeCicco, J., Gray, A. T., & Struckmeyer, R. (2008). Verification of the VARSKIN beta skin dose calculation computer code. *Health Physics*, 94(6), 527-538.
- Shultis, J. K., & Faw, R. E. (2000). *Radiation Shielding*. La Grange Park, IL: American Nuclear Society.
- Siciliano, E. R., Ely, J. H., Kouzes, R. T., Schweppe, J. E., Strachan, D. M., & Yokuda, S. T. (2008). Energy calibration of gamma spectra in plastic scintillators using Compton kinematics. *Nuclear Instruments and Methods in Physics Research, A*, 594(2), 232-243.
- Soares, C. G., Darley, P. J., Charles, M. W., & Baum, J. W. (1991). Hot particle dosimetry using extrapolation chambers and radiochromic foils. *Radiation Protection Dosimetry*, 39(1-3), 55-59.
- Turner, J. E. (2007). *Atoms, radiation and radiation protection* (3rd ed.). Weinheim, DE: Wiley-VCH.
- Vapirev, E. I., Jordanov, T., Amin, S., Stoilov, N., & Georgieva, K. (1996). Scintillation spectroscopy for beta ray dose measurements. *Radiation Protection Dosimetry*, 64(4), 303-308.
- Vasilev, I. O., & Volodin, A. V. (1996). Use of a Scintillation Spectrometer- Dosimeter for Separately Determining Doses under Conditions with Mixed Beta and Gamma Radiation. *Measurement Techniques*, 39(7), 778-781.
- Villarreal-Barajas, J. E., Bowler, M. G., & Charles, M. W. (2003). Electron spectra measurements and Monte Carlo calculations for a Co-60 standardised hot particle source. *Radiation Protection Dosimetry*, 104(2), 113-119.
- Wolbarst, A. B. (2005). *Physics of radiology* (2nd ed.). Madison, WI: Medical Physics Publishing.

Zwinkels, J. C., Davidson, W. F., & Dodd, C. X. (1990). Optical properties of UV transmitting acrylics for use in a heavy water Cerenkov detector. *Applied Optics*, 29(22), 3240-3248.

APPENDIX

The following appendix details the MATLAB code used for host PC interface with the digital oscilloscope and pulse shape discrimination.

```

% This is the code that works with DPP 2.0

clear all

%%%%%%%%%%%%%%%%%%%%%%%%%%%%%%%%%%%%%%%%%%%%%%%%%%%%%%%%%%%%%%%%%%%%%%%% Oscilloscope Comp %%%%%%%%%%%%%%%%%%%%%%%%%%%%%%%%%%%%%%%%%%%%%%%%%%%%%%%%%%%%%%%%%%%%%%%%%

addpath('C:\Program Files (x86)\Opal Kelly\FrontPanelUSB\API-32\Matlab');
addpath('C:\Program Files (x86)\Opal Kelly\FrontPanelUSB\API-32');

if ~libisloaded('okFrontPanel')
    loadlibrary('okFrontPanel', 'okFrontPanelDLL.h');
end

%Create object
xptr = calllib('okFrontPanel', 'okFrontPanel_Construct');
xem = okusbfrontpanel(xptr);
xem = openbyserial(xem, '');

err1 = configurefpga(xem, 'C:\Mat works\DPP2\top4.bit')

% Apply Reset
setwireinvalue(xem,16,4,4);
updatewireins(xem);
setwireinvalue(xem,16,0,4);
updatewireins(xem);

m=4e6; %number of pulses to analyze system will end when
t=0:5:5115; % m pulses are evaluated
adc=0:4095;

Th=500; %threshold value used for trigger of oscilloscope
Th=uint16(Th);

% Set the threshold
setwireinvalue(xem,17,Th,65535);           % Ch 1
setwireinvalue(xem,18,Th,65535);           % Ch 2

% Set the gain
gain=2000;
setwireinvalue(xem,8,24,65535);           %Ch 1
setwireinvalue(xem,9,gain*16,65535);
updatewireins(xem);
activatetriggerin(xem,64,0);

setwireinvalue(xem,8,27,65535);           %Ch 2
setwireinvalue(xem,9,gain*16,65535);
updatewireins(xem);
activatetriggerin(xem,64,0)

```

```

% Set the offset
off = 2000;
setwireinvalue(xem,8,25,65535);          %Ch 1
setwireinvalue(xem,9,(off)*16,65535);
updatewireins(xem);
activatetriggerin(xem,64,0);

setwireinvalue(xem,8,26,65535);          %Ch 2
setwireinvalue(xem,9,(off-90)*16,65535);
updatewireins(xem);
activatetriggerin(xem,64,0);

% Set the coincidence threshold (in cycle unit)
coin_th =10;
setwireinvalue(xem,16,coin_th*8,2040);

% Set the RUN MODE
% Run Mode = 0 : Free Running
% Run Mode = 1 : Synchronized
run_mode = 0;
setwireinvalue(xem,16,run_mode*2048,14336);

% RunSys High
setwireinvalue(xem,16,1,1);      % Ch 1
%setwireinvalue(xem,16,2,2);      % Ch 2
updatewireins(xem);

valid=0;
p=0;
%%%%%%%%%%%%%%%%%%%%%%%%%%%%%%%%%%%%%%%%%%%%%%%%%%%%%%%%%%%%%%%%%%%%%%%%

%%%%%%%%%%%%%%%%%%%%%%%%%%%%%%%%%%%%%%%%%%%%%%%%%%%%%%%%%%%%%%%%%%%%%%%% Pulse Shape Discrimination Comp %%%%%%%%%

counter_Bc400=0; %Counter for the number of pulses/contributions
counter_Bc444=0;
counter_CaF2=0;

energy_Bc400=zeros(1,m); %allocate memory
energy_Bc444=zeros(1,m);
energy_CaF2=zeros(1,m);

%%%%%%%%%%%%%%%%%%%%%%%%%%%%%%%%%%%%%%%%%%%%%%%%%%%%%%%%%%%%%%%%%%%%%%%% Components Needed For Energy Analysis %% %%%%%%%%%

bins_Bc400=1000; %number of energy bins
bins_Bc444=1000;
bins_CaF2=1000;

max_Bc400=3.5e3; %maximum integral value
max_Bc444=6e4;
max_CaF2=2.8e5;

```

```

binstep_Bc400=0:max_Bc400/(bins_Bc400-1):max_Bc400; %specify energy per
bin
binstep_Bc444=0:max_Bc444/(bins_Bc444-1):max_Bc444;
binstep_CaF2=0:max_CaF2/(bins_CaF2-1):max_CaF2;

%%%%%%%%%%%%%%%%%%%%%%%%%%%%%%%%%%%%%%%%%%%%%%%%%%%%%%%%%%%%%%%%%%%%%%%%

T1=10; %number of samples that I will integrate to use the fast/slow
ratio
T2=60;
T3=750;

%%%%%%%%%%%%%%%%%%%%%%%%%%%%%%%%%%%%%%%%%%%%%%%%%%%%%%%%%%%%%%%%%%%%%%%% Components Needed For Extrapolation Method %%%%%%%%%

tau1=20;          %decay time of fast scintillator (ns)
tau2=285;         %decay time of medium scintillator (ns)
tau3=940;         %decay time of slower scintillator (ns)
t1=tau1*4;        %integration time for fast scintillator (ns)
t2=tau2*4;        %integration time for medium scintillator (ns)
t3=tau3*4;        %integration time for slower scintillator (ns)

limit_CaF2=6e4; %threshold values to determine if legit or illegit
limit_Bc444_1=8e3;
limit_Bc444_2=3e4;

% syms t %set 't' as the variable we are integrating over
slow_int_0_t3=922.7833; %double(int(exp(-t/tau3), t, 0, t3))
slow_int_t2_t3=262.3145; %double(int(exp(-t/tau3), t, t2, t3))

med_int_0_t2=279.7800; %double(int(exp(-t/tau2), t, 0, t2))
med_int_t1_t2=210.0273; %double(int(exp(-t/tau2), t, t1, t2))

x=1:1024;

tic % to calculate real time
while valid ~=m;
    p=p+1;

    updatewireouts(xem);
    pt=getwireoutvalue(xem,32);
    while bitand(pt,1) ==0
        updatewireouts(xem);
        pt=getwireoutvalue(xem,32);
    end

    if(m==valid+1)
        setwireinvalue(xem,16,0,3);
        setwireinvalue(xem,16,0,14336);
        updatewireins(xem);

```

```

end

buf_1 = readfrompipeout(xem,160,2048); %CH 1
for k=1:1024
    j=k*2;
    data1(k)=uint16(buf_1(j))*256 + uint16(buf_1(j-1));
end

data1=double(data1);

valid=valid+1

baseline=mean(data1(1,50:80)); % take average of baseline
threshold=baseline-50; %set trigger threshold

for a=1:1024

    if (data1(1,a)<threshold) && (a>90) && (a<120)

        % integrate baseline
        baseline_integrated_1=baseline*(T1+1);
        baseline_integrated_2=baseline*(T2+1);
        baseline_integrated_3=baseline*(T3+1);

        %whole pulse not integrated only part for slow/fast ratio
        S1=baseline_integrated_1-sum(data1(1,a:a+T1));
        S2=baseline_integrated_2-sum(data1(1,a:a+T2));
        S3=baseline_integrated_3-sum(data1(1,a:a+T3));

        FCR=S1/S2; %calculate fast and slow ratios
        SCR=(S2-S1)/(S3-S1);

        data2=baseline-data1(1,:); %subtract the baseline

        S_t2_t3=5*sum(data2(1,(a+t2/5):(a+(t3/5)))); %sum up slow
only

        % integrate slow fit
        estimated_CaF2=S_t2_t3*(slow_int_0_t3/slow_int_t2_t3);

        % sum up medium only
        S_t1_t2=5*sum(data2(1,(a+t1/5):(a+(t2/5))));

        % integrate medium fit
        estimated_Bc444=S_t1_t2*(med_int_0_t2/med_int_t1_t2);

        % integrate fast pulse
        baseline_integrated_4=baseline*(t1/5+1);
        sum_Bc400=baseline_integrated_4-sum(data1(1,a:a+t1/5));

```

```

% integrate medium pulse
baseline_integrated_5=baseline*(t2/5+1);
sum_Bc444=baseline_integrated_5-sum(data1(1,a:a+t2/5));

% integrate slow pulse
baseline_integrated_6=baseline*(t3/5+1);
sum_CaF2=baseline_integrated_6-sum(data1(1,a:a+t3/5));

% falls into boundaries
if FCR>0.10 && FCR<0.40 && SCR>0.10 && SCR<0.33
    counter_CaF2=counter_CaF2+1;
    energy_CaF2(counter_CaF2)=sum_CaF2;

elseif FCR>0.10 && FCR<0.40 && SCR>0.40
    counter_Bc444=counter_Bc444+1;
    energy_Bc444(counter_Bc444)=sum_Bc444;

elseif FCR>0.70
    counter_Bc400=counter_Bc400+1;
    energy_Bc400(counter_Bc400)=sum_Bc400;

else % if not then use the pulse-fitting method

    if estimated_CaF2 >= limit_CaF2 % compare integral of
slow
        counter_CaF2=counter_CaF2+1; % fit to threshold
        energy_CaF2(counter_CaF2)=sum_CaF2;

        % calculate the intensity for any sample
        I(1,:)=S_t2_t3*exp(-x.*5/tau3)/slow_int_t2_t3;

        % shift intensity to overly actual pulse
        I(1,:)=[zeros(1,(a)) I(1,1:(1024-a))];

        % now take the difference, if Bc444 present, should
be positive
        diff(1,:)=data2(1,:)-I(1,:);

        % integrate the difference
        potential_Bc444=sum(diff(1,a:(a+t2/5)));

        % compare difference to threshold value
        if (5*potential_Bc444) >= limit_Bc444_2
            counter_Bc444=counter_Bc444+1;
            energy_Bc444(counter_Bc444)=potential_Bc444;

            energy_CaF2(counter_CaF2)=estimated_CaF2/5;

        end

        % if not then compare integral of medium to threshold
elseif estimated_Bc444 > limit_Bc444_1

```

```

        counter_Bc444=counter_Bc444+1;
        energy_Bc444(counter_Bc444)=sum_Bc444;

    end
end

break

end
end
end
pulse_count_time=toc % for real time measurement
background_count_time=178930; % background count time

% background spectra
load('C:\Mat works\background_Bc400_1000bins_2')
load('C:\Mat works\background_Bc444_1000bins_2')
load('C:\Mat works\background_CaF2_1000bins_2')

% make spectrum and subtract background
spect_w_back_Bc400=hist(energy_Bc400,binstep_Bc400);
spect_wo_back_Bc400=spect_w_back_Bc400(1,:)-...
    ((background_spectrum_Bc400(1,:))...
    /background_count_time)*pulse_count_time);
spect_w_back_Bc400(1)=0;
spect_w_back_Bc400(bins_Bc400)=0;
spect_wo_back_Bc400(1)=0;
spect_wo_back_Bc400(bins_Bc400)=0;
spect_wo_back_Bc400=round(spect_wo_back_Bc400);

% make spectrum and subtract background
spect_w_back_Bc444=hist(energy_Bc444,binstep_Bc444);
spect_wo_back_Bc444=spect_w_back_Bc444(1,:)-...
    ((background_spectrum_Bc444(1,:))...
    /background_count_time)*pulse_count_time);
spect_w_back_Bc444(1)=0;
spect_w_back_Bc444(bins_Bc444)=0;
spect_wo_back_Bc444(1)=0;
spect_wo_back_Bc444(bins_Bc444)=0;
spect_wo_back_Bc444=round(spect_wo_back_Bc444);

% make spectrum and subtract background
spect_w_back_CaF2=hist(energy_CaF2,binstep_CaF2);
spect_wo_back_CaF2=spect_w_back_CaF2(1,:)-...
    ((background_spectrum_CaF2(1,:))...
    /background_count_time)*pulse_count_time);
spect_w_back_CaF2(1)=0;
spect_w_back_CaF2(bins_CaF2)=0;
spect_wo_back_CaF2(1)=0;
spect_wo_back_CaF2(bins_CaF2)=0;
spect_wo_back_CaF2=round(spect_wo_back_CaF2);

```

```
subplot(3,2,1)
semilogy(binstep_Bc400,spect_w_back_Bc400)
title('Bc400 with background')
ylabel('Counts')
subplot(3,2,2)
semilogy(binstep_Bc400,spect_wo_back_Bc400)
title('Bc400 without background')
ylabel('Counts')
subplot(3,2,3)
semilogy(binstep_Bc444,spect_w_back_Bc444)
title('Bc444 with background')
ylabel('Counts')
subplot(3,2,4)
semilogy(binstep_Bc444,spect_wo_back_Bc444)
title('Bc444 without background')
ylabel('Counts')
subplot(3,2,5)
semilogy(binstep_CaF2,spect_w_back_CaF2)
title('CaF2 with background')
ylabel('Counts')
subplot(3,2,6)
semilogy(binstep_CaF2,spect_wo_back_CaF2)
title('CaF2 without background')
ylabel('Counts')

% deconstruct object
calllib('okFrontPanel', 'okFrontPanel_Destruct', xptr);
```

